Scrape Off Layer (SOL) transport and filaments characteristics in high density tokamak regimes

N. Vianello[1], D. Carralero[2,3], C. K. Tsui[4,5], V. Naulin[6], M. Agostini[1], I. Cziegler[10], B. Labit[5], C. Theiler[5], E. Wolfrum[3], D. Aguiam[7], S. Allan[8], M.Bernert[3], J. Boedo[4], S. Costea[9], H. De Oliveira[5], O. Fevrier[5], J. Galdon-Quiroga[11], G. Grenfell[1], A. Hakola[12], C. Ionita[9], H. Isliker[13], A. Karpushov[5], J. Kovacic[14], B. Lipschultz[10], R. Maurizio[4], K. McClements[8], F. Militello[8], A. H. Nielsen [6], J. Olsen[6], J. J. Rasmussen[6], T. Ravensbergen[16], H. Reimerdes[5], B. Schneider[9], R. Schrittwieser[9], E. Seliunin[7], M. Spolaore[1], K. Verhaegh[10], J. Vicente[7], N. Walkden[8], W. Zhang[3], the ASDEX Upgrade Team[3], the TCV Team[17], and the EUROfusion MST1 Team[18]

[1]Consorzio RFX (CNR, ENEA, INFN, Universitá di Padova, Acciaierie Venete SpA), Corso Stati Uniti 4, 35127 Padova, Italy, [2]CIEMAT Laboratorio Nacional de Fusión, Madrid, Spain, [3]Max-Planck-Institut für Plasmaphysik, Garching, Germany, [4]Ecole Polytechnique Fédérale de Lausanne (EPFL), Swiss Plasma Center (SPC), CH-1015 Lausanne, Switzerland, [5]UCSD, La Jolla, USA, [6]DTU, Lyngby, Denmark, [7]IPFN, Instituto Superior Técnico, Lisboa, Portugal, [8]CCFE, Culham Science Centre, Abingdon OX14 3DB, UK, [9]Institute for Ion Physics and Applied Physics, Innsbruck, Austria, [10]York Plasma Institute, University of York, UK, [11]University of Seville, Seville Spain, [12]VTT, Espoo, Finland, [13]Aristotle University of Thessaloniki, Greece, [14]Jozef Stefan Institute, Ljubljana, [16]DIFFER—Dutch Institute for Fundamental Energy Research, Netherlands, [17]See the author list S. Coda et al 2017 Nucl. Fusion 57 102011, [18]See the author list H. Meyer et al 2017 Nucl. Fusion 57 102014

E-mail: nicola.vianello@igi.cnr.it

Abstract. A detailed cross-device investigation on the role of filamentary dynamics in high density regimes has been performed within the EUROfusion framework comparing ASDEX Upgrade (AUG) and TCV tokamaks. Both devices have run density ramp experiments at different levels of plasma current, keeping toroidal field or q_{95} constant in order to disentangle the role of parallel connection length and the current. During the scan at constant toroidal field, in both devices SOL profiles tend to develop a clear Scrape Off Layer (SOL) density shoulder at lower edge density whenever current is reduced. The different current behavior is substantially reconciled in terms of edge density normalized to Greenwald fraction. During the scan at constant q_{95} AUG exhibits a similar behaviour whereas in TCV no signature of upstream profile modification has been observed at lower level of currents. The latter behaviour has been ascribed to the lack of target density roll-over. The relation between upstream density profile modification and detachment condition has been investigated. For both devices the relation between blob-size and SOL density e-folding length is found independent of the plasma current, with a clear increase of blob-size with edge density normalized

to Greenwald fraction observed. ASDEX Upgrade has also explored the filamentary behaviour in H-Mode. The experiments on AUG focused on the role of neutrals, performing discharges with and without the cryogenic pumps, highlighting how large neutral pressure not only in the divertor but at the midplane is needed in order to develop a H-Mode SOL profile shoulder in AUG.

PACS numbers: 52.25.Xz, 52.35.Ra, 52.35.We, 52.70.Ds
To be Submitted to: *Nucl. Fusion*

1. Introduction

Plasma Wall Interaction (PWI) is a subject of intense study in the context of fusion energy research for the understanding of the amount of heat loads, tritium retention, and the lifetime of different Plasma Facing Components. In recent years great efforts have been devoted to the interpretation of Scrape Off Layer (SOL) transport, with clear impact also on the design of future machines [1]. Transport in the SOL region, resulting from a competition between sources and parallel and perpendicular losses, is dominated by the presence of intermittent structures or filaments, which strongly contribute to particle and eventually energy losses both in L- and H-mode regimes. The role of convective radial losses has become even more important due to its contribution to the process of profile broadening also known as *shoulder formation* in L-Mode, describing the progressive flattening of the density scrape off layer profile at high density [2, 3, 4, 5, 6, 7, 8, 9] where future devices are expected to routinely operate. This increased radial transport could pose serious problems for Plasma Facing Components, enhanced by the recent observation that whenever flatter density profiles are established an increase of heat transport associated to filaments is observed in the far SOL, with filaments carrying up to 1/5 of the power ejected at the separatrix [10]. Preliminary investigations suggested that similar mechanisms occur in H-Mode as well [11, 12, 13, 14, 15] and that filaments strongly contribute to power balance and SOL transport also in the so-called H-mode density limit (HDL) [16, 17]. The present contribution will report results of a coordinated effort within the EUROfusion Medium Sized Tokamaks (MST1) framework between the ASDEX Upgrade (AUG) and TCV tokamaks, to address the role of filamentary transport in high density regimes both in L- and H-Mode. Similar methodology and techniques applied to largely different tokamaks, from a machine with a closed divertor, metallic first wall and cryogenic pumping system, to a carbon machine with a completely open divertor, allows the consistent comparison of the results from the two devices. The experimental investigation presented hereafter will try to shed a light on different scientific uncertainties concerning the SOL density shoulder formation: is shoulder formation really associated to a filamentary transport regime transition? Which is the relation between gas fueling, divertor collisionality and divertor detachment with the upstream profile modifications? Which is the role played by neutrals? To answer these questions the mechanism of shoulder formation and the role of filamentary transport have been tested against variations of plasma current and parallel connection length, and divertor neutral densities in H-Mode, through modification of cryogenic pump efficiency.

The paper is organized as follow: in section 2 a brief description of the devices and diagnostics used will be presented. Afterwards the results obtained in two different current scans, respectively at constant toroidal field and at constant q_{95} will be described in section 3 providing information on both target and upstream profiles evolution and linking them to the properties of the turbulent filaments in the SOL. In section 4 we will report the experimental investigation carried out on ASDEX Upgrade concerning the

role of neutrals in establishing the density shoulder in H-Mode extending the preliminary results reported in [15] at higher heating power and neutral pressure. Finally, in section 5 we will draw the conclusion and make an attempt towards a possible unified picture.

2. Machine and diagnostic description

2.1. ASDEX Upgrade

ASDEX Upgrade is a medium sized divertor tokamak with major and minor radii of $R = 1.65$m and $a = 0.5$m, respectively, and equipped with a fully tungsten coated wall [18]. The experimental investigation has been carried out in Lower Single Null (LSN) configuration, with the ion $\mathbf{B} \times \nabla B$ drift pointing towards the X-point. The plasma shape has been tailored to follow the shape of the outer limiter (in a configuration dubbed *Edge Optimized Configuration*), and at the midplane up to 45 mm from the separatrix the field lines are connected to the divertor target. In Figure 1 (a) the layout of the principal diagnostics used for the present analysis is shown in the poloidal cross-section. SOL density profiles are obtained from the lithium beam (LiB) diagnostic, observing the plasma at a vertical position approximately 30 cm above the midplane. Density profiles are obtained from the light emission profile, which is sampled with 200 kHz [19], and evaluated within the probabilistic Bayesian framework [20] with 1 kHz in the radial region spanning approximately $0.9 \lesssim \rho \lesssim 1.05$, ρ being the normalized poloidal flux. In the core and at the edge line densities are obtained with the standard interferometer system shown as well in Figure 1. The principal diagnostic used for investigating the fluctuations is the midplane manipulator (MEM) equipped with a tungsten coated carbon probe head designed to characterize turbulence and simultaneously withstand the high heat flux observed in H-Mode. The probe features 16 pins distributed among 3 terraces at different radial position (radial separation is 4 mm) whereas the different arrays are aligned in the bi-normal direction as described in [21] with typical distances of 6 mm. The pins are arranged to measure both floating potential and ion saturation current: in particular the ion saturation current pins are distributed in order to have measurements spaced both in the radial and in the poloidal direction which allow a proper estimate of the radial and bi-normal velocities using a 2D cross-correlation algorithm described in the appendix of [21]. Several plunges can be done within a single pulse. For the L-Mode shots presented hereafter up to 5 plunges were performed with the probe sitting in a fixed position for up to 130 ms. In the H-Mode operation the time duration of the fixed position was reduced to 70 ms to limit the heat load deposition on the probe head. The acquisition sampling rate for all the shots was set to 2 MHz, which give us relatively long time series for turbulence analysis. In addition one pin is run in swept mode in order to infer the local estimate of density and electron temperature. The information on divertor conditions are primarily obtained by two arrays of fixed flush mounted triple Langmuir probes, shown in Figure 1 by red circles, sampled at low sampling rate (33 kHz).

2.2. TCV

The Tokamak à configuration variable (TCV) is a medium sized tokamak located at the Swiss Plasma Center, Switzerland [22]. It is a conventional aspect ratio tokamak (major and minor radii $R = 0.88$ m and $a = 0.25$ m, respectively) with a highly elongated vacuum vessel and a completely open divertor. TCV features 16 independently powered poloidal field coils, resulting in unique shaping capabilities, with the ability to accommodate highly elongated plasmas (up to 2.8) and triangularity in the range $-0.7 \leq \delta \leq 1$. The near-complete coverage of TCV surfaces with graphite tiles allows extreme flexibility in power load deposition, making TCV an ideal test-bed for the study of different magnetic configurations and divertor geometries.

In recent years great efforts have been devoted in TCV to increase the diagnostic equipment for divertor studies. A new 32-chords divertor spectroscopy system (DSS) [23] has been installed for extracting information on recombination and electron temperature from Balmer series spectra. This information can be combined with radiation measurements estimated from Bolometry [24]. An array of wall-mounted Langmuir probes (LPs) [25] covers the inner and outer wall as well as the floor. The cylindrical tips have diameters of 4 mm and are embedded into the tiles except at the floor where they have a dome-shaped head protruding from the tile shadow by 1 mm. For the present experiment the probes have been operated in swept mode to obtain density and temperature profiles at the wall. The set of LPs has been extended by the installation of a fast reciprocating probe (RCP) [26]. The probe head, described in detail elsewhere [27], is equipped with 10 graphite electrodes 1.5 mm in diameter. The electrodes are arranged in such a way to provide a double probe for density and temperature profiles, two Mach probes for parallel flow investigations, a pin for fast ion saturation current measurements with the remaining probes collecting floating potential in order to infer radial and poloidal electric field fluctuations from the local floating potential gradient. The radial separation between the floating potential pins is 1.57 mm whereas the poloidal separation between the pins are 4 mm and 10 mm respectively. The fast movement of the probe head is 20 cm which is reached within 90 ms with a maximum speed of 2.2 m/s. The ion saturation current and floating potential electronics have a bandwidth from 0.1 to 10 MHz with anti-aliasing filters at the Nyquist frequency: the acquisition frequency was set between 1 MHz to 5 MHz for different discharges used throughout the paper. The profiles in the SOL have been obtained combining the data from RCP with the ones from Thomson scattering diagnostic obtained in adjacent time instants: for TCV the profiles shown throughout the paper have been fitted using a Gaussian Process regression technique (details can be found in [28] together with the link to the available software tool). The method allows for a proper determination of the fit and corresponding errors, as well as of the density gradient with the corresponding errors. This will be used throughout the paper to compute the e-folding length profile shown in the following figures. The Line of Sights (LOS) of bolometry, the location of the Langmuir probes and of the reciprocating manipulator used throughout the paper

and the LOS of the vertical Far Infrared interferometer for edge and central chord are shown in Figure 2 to provide an idea of the spatial resolution of the diagnostic setup. The combined information provide a comprehensive set of measurements suited for the divertor investigation.

3. L-mode Current scan

The dependence of the SOL density profile on plasma current in L-mode has been previously reported [2, 5, 6, 8] both for closed and open diverted devices. In all the cases it has been shown that flatter profiles in the Scrape Off Layer develop at lower densities for lower currents. Following this premise the first set of experiments was conceived to disentangle the role played by plasma current variation from the changes in parallel connection length and consisted of two series of L-mode density ramps, up to disruption, at different current levels keeping respectively the toroidal field or the q_{95} constant.

3.1. Divertor target evolution

Figure 3 reports the main plasma parameters concerning the current scan at constant toroidal field both for AUG and TCV. The 3 levels of plasma current for the two devices as well as the edge line integrated density and the fuelling levels used for the discharges are shown. The parallel connection lengths $L_{\parallel}$, shown in panels (a) and (g) of Figure 3, are the connection lengths from the outer target up to the X-point height, and clearly increase with decreasing current for both the devices. TCV discharges are purely Ohmic plasmas, whereas on AUG an additional 0.5 MW of NBI heating was added in order to keep a similar heating power through the separatrix during the scans. Still in Figure 3, panels (e) and (m), the power crossing the separatrix, estimated as $P_{sep} = P_{\Omega} + P_{heat} - P_{rad,core}$, is reported for the various current levels for both devices. Clearly the additional heating allows to keep much more comparable power levels for AUG. The divertor pressure on TCV, as seen from panel (n) of Figure 3 measured by baratrons, does not exhibit differences between the various current levels. On AUG, where fast gauges located closer to the vessels are used, slightly higher pressure are achieved at higher current (cfr panel(f) of Figure 3) [21].

The first relevant information can be derived by considering the response of the divertor to different density levels at different current. In Figure 4 the total integrated ion fluxes to the outer divertor are shown as a function of edge density and edge Greenwald fraction (i.e. edge density, obtained from interferometric edge chord, normalized to Greenwald density value n_e^e/n_G) for AUG (panel (a) and (b)) and TCV ((e) and (f)), respectively. The choice of normalization (edge density normalized to Greenwald density) is done in order to consider possible effects due to the different density peaking obtained at different edge safety factor [29]. As already observed the integrated ion flux in TCV increases almost linearly with the density up to the threshold

followed by a smooth roll-over [30], the latter assumed in the following as a proxy for plasma detachment. Differently in AUG the increase of ion flux is faster than linear up to the threshold with a more pronounced roll-over. These differences are likely due to the different degree of divertor closure [31]. In both devices we clearly see that ion flux roll-over occurs early in edge density at lower current. In AUG, where the power crossing the separatrix is a factor of 2 higher, the behaviour at different current is reconciled in terms of edge Greenwald fraction. The same observation holds for the two lower currents in TCV, whereas higher edge Greenwald fraction is needed for the higher plasma current. In the scan shown in Figure 3, where the density increase was kept similar at different values of current, indeed no detachment of the outer leg has been achieved for the higher current case: conversely whenever the density is increased even further, as the case of shot # 52065 reported as well in panel (e) and (f) of figure 4, clear outer leg detachment has been obtained even though at higher density. In the same figure 4 the behaviour of the inner divertor legs for both the devices is shown . In AUG the integrated ion flux is much lower even though the behaviour in term of edge density resembles what is observed in the outer divertor. On TCV the integrated ion flux to the inner divertor is larger and exhibits a less pronounced roll-over at the lower current levels explored, whereas no sign of roll-over is observed at higher current. It is worth noting that, differently from AUG, inner target generally detaches later than the outer one in TCV [32, 30], and this has been observed in K-STAR as well [33]. It is worth noting that both K-STAR and TCV are carbon machines, with the inner strike point on a vertical target and a short poloidal distance to the X-point and an outer strike point on an horizontal plate with a much longer poloidal distance from the X-point. In both the machines the presence of carbon impurities could increase the pressure and power dissipation with respect to the pure D case. In particular carbon radiation is a strong power loss channel but an additional indirect effect in the pressure balance may happen: the carbon induced cooling and consequent reduction of the electron temperature can indirectly increase the momentum loss and increase the volumetric reaction rates which are responsible themselves for momentum loss. Work is in progress within a 2D fluid SOL modelling effort for TCV to properly account for these contribution in similar plasmas [34]. In any case a close comparison of the detachment operational space between the two devices is beyond the scope of the present paper and will be eventually addressed in further investigations.

A similar current scan has been performed varying the toroidal field together with the current in order to keep q_{95} constant: the corresponding main plasma parameters are shown in Figure 5 for both devices. From panels (a) and (g) we noticed that $L_{\parallel}$ was kept constant throughout the current scan, even though slight variations are observed in TCV at the lower current level. For the sake of completeness we need to underline that at the lower current level we had to operate TCV at an unusually low toroidal field ($B_t \approx 0.8$ T). The time evolution of the aforementioned P_{SOL} and of the divertor neutral pressure are shown in Figure 5 for both the devices. Again, the heating scheme used (pure Ohmic discharges for TCV and additional 0.5MW of NBI heating in AUG)

allows to keep the P_{SOL} approximately constant in AUG. The pressure in the divertor is constant throughout the scan in TCV whereas slightly higher pressure is achieved at higher current in AUG. The evolution of total ion flux at the outer and inner divertor as a function of edge density and edge Greenwald fraction are shown in figure 6. For AUG in analogy to the observations obtained during the scan at constant toroidal field, the ion flux roll-over is observed at lower density for lower current but the behaviour is reconciled in terms of edge Greenwald fraction for both inner and outer divertor. On the other hand the comparison of shots at similar current but different toroidal field (e.g. # 34104 and 34106) reveals that the rollover density threshold is essentially unmodified by the variation of $L_{\|}$, but a more robust and faster reduction of ion flux just after the roll-over is obtained at larger $L_{\|}$. On TCV instead no sign of detachment neither at inner nor at the outer divertor was observed, even though the achieved density was sufficient to guarantee plasma detachment whenever the same density ramp was run at higher toroidal field (compare Figure 6 panel (e) with the same panel of Figure 4). This is an interesting observation which does not seem to be due to a change in the power crossing the separatrix since the values of P_{sep} at the same current are comparable at least around the time where higher field discharge exhibits ion flux roll over as can be inferred by comparing Figure 3 and Figure 5. The understanding of the differences at lower toroidal field is presently under investigation.

3.2. Upstream profile evolution

Figures 7i and 7ii report the evolution of the upstream profiles for different current levels at the same value of edge density and toroidal field for AUG and TCV respectively. In the same figures we have also included the density profiles at the outer target (panels (c) and (d) of sub-figures 7i and 7ii) as well as the profiles of the normalized collisionality Λ defined as :

$$\Lambda = \frac{L_{\|}\nu_{ei}}{c_s}\frac{\Omega_i}{\Omega_e} \tag{1}$$

This quantity represents an effective collisionality or equivalently the ratio between the parallel transit time divided by the inverse of the electron-ion collision frequency. It has been originally introduced in [35] and adopted in [7] as a parameter to identify enhanced filamentary transport transition in high density regimes. In particular in [7] it has been suggested that filamentary transport enhancement is regulated by the effective collisionality in the divertor, Λ_{div}, which depends on the parallel connection length, evaluated as the length from the X-point height to the outer target, and on the values of density and temperature in the divertor region, estimated in the present paper from target density and temperature given by Langmuir probes at the outer target. In the following all data will be presented as function of divertor collisionality Λ_{div}. The error bars on Λ_{div} shown throughout the paper have been estimated propagating the errors on the target density and temperature. It can be easily observed that flatter profiles are obtained at lower current for the same density levels for both the devices even though

some differences may be noted. In AUG the different upstream profiles are associated to different target density profiles and clearly different divertor collisionality. All the cases where the profiles in AUG at the outer midplane are flatter are associated to higher values of divertor collisionality. Differently outer divertor collisionality does not represent a proper metric for TCV since very different upstream profiles are obtained with comparable Λ_{div} profiles even well above the threshold of $\Lambda_{div} \gtrapprox 1$ identified in [7] for increased filamentary transport regimes: this confirms previous observations [9] where a variation of divertor collisionality obtained through modification of target flux expansion has shown little impact on evolution of upstream profiles. On the other hand we have already observed that, apart from the TCV case at higher current, edge Greenwald fraction can reconcile the target profiles evolution. Figures 8i and 8ii compare again upstream and target profiles, as well as divertor collisionality at comparable edge Greenwald fraction but different current levels for both the devices. We clearly recognize that the upstream profile evolution behavior at different current is better reconciled in terms of edge Greenwald fraction, with similar shoulder developed at comparable n_e^e/n_G

The investigation of the target evolution with edge density in the current scan performed at constant q_{95}, shown in Figure 6 already revealed differences between AUG and TCV, in particular showing that the reduction of toroidal field prevent the plasma from reaching a detached condition in TCV at lower current. This reflects also to different upstream behaviour as shown in Figure 9 (i) and (ii) respectively for AUG and TCV. Indeed while for AUG the behaviour at constant q_{95} reflects what was observed at constant toroidal field, with substantial overlap of target and upstream profiles at equivalent values of edge Greenwald fraction, the behaviour of TCV is scattered with a clear shoulder developed only at high current, were also the broader target profile is recognized. We can also confirm that the evolution of the upstream profile is independent of the evolution of Λ_{div} as computed at the outer divertor. Investigation is in progress on TCV in order to eventually understand the dependence of shoulder formation on the divertor collisionality computed at the inner divertor, Λ_{div}^{inn}. Indeed, the inner divertor, with its shorter connection length $L_{\parallel}$ with respect to the outer divertor one, could exhibit a largely different value of Λ_{div}^{inn}, with lower values at similar edge densities.

In order to properly understand the relation between upstream to downstream condition we have monitored the evolution of upstream profile with respect to detachment condition. This can be done within a single shot on AUG, due to the availability of time resolved SOL density profiles through LiB, whereas for TCV we had to rely on repetition of similar shots, namely 330 kA L-mode plasma with the same density ramp, where the reciprocating probe head has been plunged at different times. The result of this analysis is shown in Figure 10 where upstream profiles, normalized to the value at the separatrix are shown for different levels of detachment. The obtained profiles suggest that the modification of the upstream profiles for both of the devices begin close to the ion roll-over and further develop as soon as the ion flux starts decreasing. For completeness it should be pointed out that the chosen scenario for shot repetition on TCV, at 330 kA, is the one which requires higher edge Greenwald

fraction to exhibit ion flux roll-over. A more refined and detailed analysis of the relation between ion-flux rollover and upstream profile modification on TCV, including cases where detachment is achieved by pure N_2 seeding, will be addressed in a forthcoming paper [36]. As far as TCV is concerned, from the present dataset we can confirm that, if detachment is achieved by pure fueling and intrinsic impurity radiation, upstream profile variation are observed only close to and after ion-flux rollover.

3.3. Influence of neutrals on shoulder formation

Even though the increase of filamentary convective transport has been recognized since the beginning [4] to play a fundamental role in the process of shoulder formation, the role of other mechanisms is presently under consideration. Among them, the influence of neutrals in the divertor region, which has been theoretically proposed [37] and experimentally suggested in [38] is subject of intense study. On the other hand also the role of neutrals in the main chamber which could modify the ionization rate in the Outer Midplane (OMP) has been proposed as a possible candidate in the process of shoulder formation [15], even though it is still debated [8].

This motivated an activity to determine the emission of neutral deuterium in the divertor region on AUG, based on the evaluation of signals collected by two cameras with two different filters for D_α (656 nm) and D_γ (434 nm) lines, respectively. The two absolutely calibrated cameras [39] are both located just below the midplane (Z=-0.27) at slightly different toroidal angle (the centre of the two cameras are shifted by 6 toroidal degrees and they both observe the same divertor region). A tomographic algorithm has been developed in order to infer the 2D map of the emissivity ϵ. Assuming toroidal symmetry, the emission is a function of radial and vertical positions only, i.e. $\epsilon = \epsilon(R, Z)$. This allows us to to project each Line of Sight (LoS) corresponding to each camera pixel in the plane (R, Z) [40]. In this plane the different LoSs intersect each other, allowing for the development of a proper tomographic reconstruction. In order to introduce as little as possible a-priori constraints, the pixel method is used, and the inversion is performed with an iterative algorithm. Two assumptions are made: D_α and D_γ emissions do not depend on the toroidal angle, and they are restricted to the region outside the separatrix. Thus the divertor region outside the separatrix is divided into rectangular pixels and the emissivity ϵ in each pixel is considered constant. Using this method, the link between the intensity measured by each LoS of the camera and the emissivity is a linear system of equations, that can be written as:

$$\mathbf{I} = \mathbf{A} \cdot \epsilon \tag{2}$$

where I_j is the line integrated signal measured by the LoS j; ϵ_i is the unknown emissivity of the pixel i; and the matrix element a_{ij} is the length of the LoS j inside the pixel i. This matrix is evaluated only once, and it depends on the geometry of the LoS and the pixels division. In eq. 2 there are ≈ 40000 LoSs and ≈ 200 pixels, so the system is over-determined. For inverting it and obtaining the emissivity of each pixel, the simultaneous algebraic reconstruction technique (SART) is used [41, 42]. It is an iterative technique

which solves the linear system of Eq. 2 via an iterative error-correcting procedure, which can be written as:

$$\epsilon_i^{k+1} = \epsilon_i^k + \frac{\Sigma_j \left[a_{ij} \frac{\mathbf{I}_j - \mathbf{a}_j \cdot \epsilon^{(k)}}{\Sigma a_{ij}} \right]}{\Sigma_j a_{ij}} \tag{3}$$

where ϵ_i^k is the emissivity of the pixel i after k iterations. The initial estimate ϵ_i^0 is set to 0. Since the emissivity of each pixel is positive, this constraint is enforced in each iteration by setting to zero the coefficients that are less than zero after an iteration step. The convergence is quite rapid, and after about 20 iterations it is reached.

The results of this analysis is shown in figure 11 where the inversions for both D_α and D_γ are shown at three different values of edge normalized Greenwald density. At the beginning emission is strongly localized in the inner divertor, consistent with the presence of a High Field Side high density region [43, 44]. During the fuelling ramp the divertor moves into a high recycling regime and D_α and D_γ radiation move towards the low field side (LFS) region, initially in the private flux region (PFR) and then in the main SOL moving upstream once the target density rolls over. This strongly resembles the observation on JET in the Horizontal Target [38]: in this configuration indeed JET upstream profile develops a clear shoulder whenever fuelling is raised, and this is accompanied by a clear D_α radiation front moving into the main LFS SOL. On the other hand whenever run in the Vertical Target configuration no shoulder is observed in JET at the same level of fuelling, and D_α radiation was confined to a narrow region along the divertor leg. This observation seems to reconcile the behaviour of JET and ASDEX Upgrade despite the different divertor configurations.

An effort is ongoing in order to use the 2D map of the emissivity of the two Balmer lines in the divertor to infer the neutral density [45]

3.4. Filamentary studies

The role of enhanced convective filamentary transport in the formation of SOL density shoulder has been already suggested [3, 4, 7, 9], even though reduced parallel losses could also influence the process. The relation between profile evolution and blob-sizes has been investigated in the present scan using properly designed probes. In both the devices the blob-size is determined as $\delta_b = \frac{\tau_b}{2} v_\perp$ with τ_b estimated as the FWHM of the conditionally averaged ion saturation current signal where peaks 2.5 standard deviation σ higher than the average values have been detected. Due to the different experimental setup of the probe head, the estimate of the perpendicular velocity is done differently in the two devices. For TCV we have used the method extensively described in [27] and the perpendicular velocity is estimated as $v_\perp = \sqrt{v^2_{r,\mathbf{E}\times\mathbf{B}} + v^2_{pol,cross-corr}}$: $v_{r,\mathbf{E}\times\mathbf{B}}$ has been estimated from the conditionally averaged sampled E_θ using as condition the detection of the peaks on ion saturation current. The fluctuating electric field is computed from the local floating potential gradients. The poloidal velocity component is estimated from the 2D cross-correlation of poloidally and radially spaced floating potential measurements

as detailed in [27]. For AUG the estimate of $v_\perp$ is done following the method described in the appendix of [21], based on the 2D cross-correlation using conditionally sampled ion saturation current structure measured by pins spaced both in the radial and poloidal direction. For a better comparison with previous results we underline that τ_b is estimated differently with respect to [27], since in the present manuscript the asymmetric shape of the ion-saturation current conditionally average sampled is kept, thus considering the trailing wake neglected in the aforementioned paper [27]. Furthermore in previous AUG papers [21, 7, 15] τ_b was approximated by the auto-correlation time, and all the data shown were actually the blob diameter, rather than the blob radii which will be shown in the present paper. In AUG the filaments are detected during the fixed positions of the probe. This implies a long signal length (up to 130 ms at 2 MHz for the L-Mode cases) where several hundreds of filaments are detected and used to infer the Conditionally Average Sample (CAS) waveforms. In TCV conversely the probe is continuously moving: the peaks on I_{sat} exceeding the chosen threshold are sampled from a 3 ms windows, as done in [46, 27] after removing the slow time evolution caused by the motion of the reciprocating probe. Several windows are sampled for each plunge at different radial insertions of the probe. Typical examples of the results obtained from the conditionally average sample technique for the two devices are shown in Figure 12. The yellow bar indicates the estimate of the FWHM: for TCV we have shown as well the typical waveform of the poloidal electric field fluctuations from the CAS. The data presented refers to a shot at low density: the shape of the ion saturation current, presented in units normalized to the rms value σ is asymmetric for both the devices, as already seen [6, 47, 48, 49] even though the total pulse length is different between the two machines. The pattern observed for AUG on the pins displaced in the radial and poloidal directions clearly recognized the intermittent structure whereas from the time-delay a proper determination of the movement in the two directions can be inferred. The observed fluctuation of the poloidal electric field for TCV is of the order of 1.5-1.8 kV/m giving a radial velocity of the order of 1.5 km/s in agreement with previous estimate [27].

As aforementioned, recent results ascribed the broadening of SOL density profile to a transition in the filamentary regime from a connected regime to a disconnected or inertial one [7, 50, 15]. A threshold has been identified with transition to inertial regimes occurring for $\Lambda_{div} \gtrsim 1$. The experimental results supporting this hypothesis have been clearly obtained in AUG and in JET, the latter device only whenever run in Horizontal Target configuration [7, 38]. But the dependence on divertor collisionality is not universally recognized: for example Λ_{div} fails to describe the operation of JET in vertical target configuration [38] as well as in TCV where very similar profiles are obtained with largely different outer target Λ_{div} values, even though, as aforementioned, the evaluation of the influence of inner divertor Λ_{div} influence is still under investigation.

In this respect we have investigated the evolution of the e-folding length of SOL density profile, defined as $\lambda_n = \left(\frac{|\nabla n_e|}{n_e}\right)^{-1}$ as a function of previously defined divertor

collisionality Λ_{div} and as a function of the blob-size δ_b. As previously mentioned the e-folding length is not computed from local exponential fit of the profiles, but rather by estimating local density gradient as a result of the fitting procedure which provide estimate of the error on the gradient as well, used then to propagate the error on the e-folding length estimate. The e-folding length is computed at the same radial location as the estimate of the blob-size, namely for $\rho \approx 1.02 - 1.03$ for AUG and $1.025 \lesssim \rho \lesssim 1.045$ in TCV. Blob dimensions are normalized to the local ion-sound gyroradius $\rho_s = \sqrt{\frac{T_e+\gamma T_i}{m_i}}$ where the assumption $T_i = T_e$ has been assumed for TCV. On AUG instead, where detailed investigation on the behavior of ion temperature in the SOL at different levels of density has been performed [10], we have assumed $T_i = 3T_e$ for $\Lambda_{divs} \lesssim 1$ and $T_i = T_e$ for larger collisionality. In order to get rid of possible uncertainties due to the scattered points, on TCV we have used the evaluation of the profile from the Gaussian-process regression fit shown in the previous figures (cf. figures 7, 8 and 9) which provide also an evaluation of the error on the radial derivative of the fit. The results of this analysis are shown in figure 13 respectively. The original trend observed in AUG [7] is confirmed in both the series of discharges with a clear increase of the e-folding length as soon as Λ_{div} increases and a strong dependence of λ_n on the blob-size. It is worth noting that within the different current levels no distinction is clearly observed.This is in agreement with observation obtained from LiB diagnostics reported in [51], where no sensible dependence of blob size on the toroidal field strength were observed both in scaling at constant I_p and constant q_{95}. The corresponding blob values, for comparable greenwald fraction are compatible with observation obtained using LiB on AUG [51] or GPI [52]. On TCV, limiting to the dataset with the same toroidal field, the e-folding length increases with blob-size (cfr figure 13 panel (g)), whereas we confirm that no dependence is observed on the outer target Λ_{div} (cf. figure 13 panel (c)). On the other hand, whenever the current is scanned keeping q_{95} constant on TCV the e-folding length is constant despite the 2 orders of magnitude of difference in Λ_{div} (cfr figure 13 panel (d)), but at the same time small variations of blob-size are observed (cf. figure 13 panel(h)). From the observation of Figure 5 we already suggested a possible link between upstream profile variation and detachment condition: during the scan at constant q_{95} no signature of detachment or ion saturation roll-over was observed (as seen in figure 6), and this analysis confirms that no variations of the upstream e-folding length, as well as small variation of blob-size are observed if no ion-flux roll-over occurs.

In order to check the dependence of the blob-size on the divertor detachment status we consider a similar set of discharges used in Figure 10 and evaluate the blob-size at different edge Greenwald density fractions. The result is shown in Figure 14. On AUG the number of plunges in a single shot prevents a detailed analysis close to the roll-over. Nevertheless we can substantially confirm that the blob-sizes are small with the plasma in attached condition, and then the size increases close to and after the roll-over. On TCV a sharp increase of blob-size is observed around $n_e^e/n_G \approx 0.3$ with a further saturation at larger edge Greenwald fraction. The same information can be obtained on a statistical basis considering all the database available for both devices. For the sake of

clarity we have included only the shots at the same toroidal field on TCV and for currents below 300 kA, where a clearer location of ion-flux roll-over is observed. The result is shown in Figure 15 panel(a): on AUG a sharp increase is observed around $n_e/n_g \approx 0.3$, which coincides as seen in figures 4 with the transition to a high-recycling regime. For TCV we observe an increase of the blob-size up to the edge Greenwald fraction $0.25 \lesssim n_e/n_G \lesssim 0.3$ where again ion-flux roll-over at the outer target is observed for currents below 330 kA. Afterwards the blob-size seems to saturate. The behaviour of the two devices is reasonably well reconciled, with an increase during the increase of the ion-flux to the outer target up to a saturation after the roll-over. For the sake of completeness it is worth mentioning that the smaller blobs on AUG have as estimated diameter at the limit of our diagnostic and method capabilities. Nevertheless the observed trend, which is consistent with past results even though obtained with a different probe head, made us confident of the reliability of the drawn conclusions. Blob size estimates from probes are based on the evaluation of the characteristic time τ_b and on the binormal velocity $v_\perp$ which can be projected into the radial and vertical motion. In Figure 15 panels (b), (c) and (d), the different contributions are shown still as a function of edge density normalized to Greenwald fraction. We clearly see that the larger variations are observed for τ_b, which increase with n_e^e/n_G in agreement with the results reported in [9], with the increase of auto-correlation time observed in AUG [21] and with similar analyses based on LiB diagnostic on AUG as well [53]. It is worth noting that these results seems to contradict observations obtained using GPI on C-Mod [48] or probe measurements still in TCV [47] where the pulse shapes of the intermittent structures were insensitive to the changes in density. So far no clear explanation of these differences has been determined. On the other hand, in the same figures we report both the radial and poloidal velocities normalized to the local ion-sound speed. For AUG a modest increase with the density is observed confirming what was shown previously using probes [21] or LiB [53]. The behavior in TCV exhibits a different trend with an almost constant value for the poloidal component and a modest decrease, if any, at higher densities on TCV: both behavior confirms previous observations [9]. On the other hand previous measurements of the effective radial velocity on TCV [47] show a small variation with density in the far SOL and a larger variation in the near SOL still compatible with present results.

Finally, in order to properly compare the filamentary features between the two devices we consider all the filaments detected in the $\Theta - \Lambda_{div}$ plane, where Λ_{div} has been already described, the parameter Θ is defined as

$$\Theta = \left(\frac{\delta_b R^{1/5}}{L_\parallel^{2/5} \rho_s^{4/5}} \right)^{5/2} \tag{4}$$

with an obvious meaning of the different quantities. Specifically for both the devices both Θ and Λ_{div} are computed considering $L_\parallel$ as the parallel connection from the outer target up to the X-point height, whereas the ion-sound gyroradius is locally computed at the position of the filament measurements. These two invariants have been originally introduced in the so called *two region* model [35]. The second invariant Θ is a typical

spatial blob scale. The proposed model allows the distinction of different regimes for the filaments where different velocity scalings with respect to filament size and different current closure schemes are identified. While a detailed description can be found in the original paper [35], for the present paper it is sufficient the distinction between filaments electrically connected to the target (in the *sheath-connect* (C_s) or in the *connected ideal interchange* (C_i) regimes) on one side and those electrically disconnected as the *resistive X-point* (RX) or the *resistive balloning* (RB) regimes on the other side. These different regimes occupy different portions in the $\Lambda - \Theta$ plane as pointed out in [35, 27]. The evaluation of Λ and Θ for all filaments detected in both devices is shown in Figure 18. In the same plot we have also marked the regions for the different regimes. Actually the boundary of the connected ideal interchange regime C_i depends on the magnetic fanning parameter ϵ_x, which is a measure of the elliptical distortion of the flux surfaces. In analogy to what was done in [27] for the plot shown in Figure 16 we have chosen a value of $\epsilon_x \approx 0.3$. As pointed out in [27] TCV blobs have features mainly consistent with a resistive ballooning type with the radial velocity which should scale as the square root of the blob size. For ASDEX Upgrade the points at very low collisionality ($\Lambda_{div} \lesssim 6 \times 10^{-2}$) appear to be close to a connected regime whereas transition to a clearly disconnected regime is achieved whenever higher collisionality is reached. Thus while in AUG different filamentary regimes seem to have been attained, in TCV in the explored collisionality region no regime variations have been observed and this could be responsible for the lack of dependence on collisionality. This could be as well the reason for the lack of dependence of the e-folding length from Λ_{div} although further investigations are indeed mandatory. Presently work is in progress to compare velocity estimates with independent measurements, such as fast camera velocimetry measurements, which will give us additional data to eventually support these considerations. Besides the determination of the filamentary regime, investigations are under way in order to quantify also the level of transport associated to the filaments at different levels of shoulder formation, in analogy to what was done in [15], since increased convective losses are ultimately responsible for the enhanced radial transport.

As already mentioned, increasing investigatory efforts have been devoted to the role of neutrals in determining the SOL profile flattening at high density, both from an experimental [8] and a numerical point of view [54, 55, 56, 57]. In this respect an attempt to distinguish the behaviour of upstream SOL e-folding length with respect to the neutral pressure as measured at the midplane or in the divertor region in AUG has been carried out, and the results are shown in Figure 19. In panels (a) and (b) of figure 17 the e-folding length, still computed around $\rho \approx 1.02 - 1.03$, is shown as a function of divertor collisionality and of blob-size respectively with a color-code representing the measurement of sub-divertor neutral pressure, whereas on panels (c) and (d) the same plot is shown with colour-code proportional to the pressure as measured by midplane gauges. The plot suggests, even though not perfectly, a general tendency of developing flatter profiles in the SOL at higher neutral pressure, with a weaker dependence on the divertor values with respect to the midplane one. This is actually interesting, and

in partial contradiction with observation in JET [38] and MAST [8]. We will address a similar analysis in TCV as well, where more robust and reliable measurements from gauges both in the divertor region and midplane will be available in a near future. What the results up to now point out clearly is that a global comprehension, which unifies the experimental observations obtained from a variety of devices, must retain the physics of interaction between plasmas and its fluctuations and neutrals.

4. H-Mode experiment

The question of whether the mechanism of SOL profile flattening is affecting also the profiles in H-Mode is a fundamental issue, since operation at high Greenwald fraction with divertor in detached condition is envisaged for future reactor-relevant plasmas. The present contribution will extend the observations already reported in [14, 15], with more detailed filamentary investigations in H-Mode plasma in AUG with a total power up to 5.8 MW and focusing on the role of divertor neutral pressure by comparing operation without and with the cryogenic pumps.

The time traces of relevant parameters are shown in figure 18 for 3 different discharges at 0.8 MA, B_t = -2.5 T in ASDEX Upgrade all with the same heating power of 5.8 MW obtained through a combination of NBI and ECRH. Shots # 34276 and 34278 were operated with the same fuelling and seeding settings without and with the cryogenic pumps, whereas for shot # 34281, where the cryogenic pump was operated, both fuelling and seeding were increased aiming to match the sub-divertor neutral pressure (panel (d) of Figure 20). It is worth noting that the level of fuelling attained in these shots and the heating power are much higher than what reported in [15]. Comparing shots #34276 with #34278 we observe that keeping the same level of fuelling and seeding but starting the cryogenic pump prevents the plasma from detachment (indicated by constant divertor temperature) with a modest increase in edge density. To reach similar conditions for edge density and detachment, high levels of fuelling and seeding are needed. Another clear difference between operation without and with the cryogenic pump is the ELM behaviour, as observed by the measurements of the divertor shunt current at the outer divertor shown in panel (f) of figure 18, with shots #34276 and #34281 exhibiting a clear reduction of the ELM amplitude and a transition toward a small ELM regime at higher density, whereas a modest reduction is observed in the shot with the lower neutral divertor pressure.

In Figure 19 the upstream and target inter-ELM profiles for the same three shots are shown for three different time instants in analogy to what was done in [15]. It is worth noting that while the determination of inter-ELM intervals is easy at the beginning of the H-Mode phase of the discharge, the distinction at a later stage, with such an high ELM frequency and low amplitude, is difficult. Nevertheless even at high density a suitable threshold on divertor shunt current has been determined in analogy to [15], even though no sensible differences were identified with respect to average profiles determined without distinction between ELM and inter-ELM intervals in the small ELM regime. This makes

us confident that the considerations carried out can be properly compared with similar measurements presented in [58]. In all cases we start from a clearly attached plasma with a steep upstream profile and a divertor collisionality completely, or at least partially, below the threshold $\Lambda_{div} = 1$. Both the target and upstream profiles start evolving for shots with comparable sub-divertor neutral pressure (# 34276 and # 34281) moving towards high recycling and finally to fully detached conditions. Consistently, the divertor becomes fully collisional with a Λ_{div} profile well above 1 in the explored radial region and the upstream profiles tend to flatten, more robustly for the shot at higher divertor neutral pressure. On the other hand for shot #34278 the upstream and target profiles remain practically unchanged with the peak target density still increasing without sign of roll-over. This is observed even though Λ_{div} increases in the near SOL, thus confirming the stronger influence of the far SOL divertor condition in determining upstream profiles in AUG [50]. In analogy to the investigation performed in L-Mode we now verify the evolution of upstream profiles in terms of divertor status. Figure 20 shows the evolution of integrated outer divertor ion flux as a function of edge Greenwald normalized density for the same shots. For shot # 34276 without the cryogenic pump, a divertor evolution similar to the one observed in L-Mode can be recognized, with the divertor moving from an attached condition, to high-recycling and then detachment after ion-flux roll-over occurring around $n_e/n_G \approx 0.7$. For the same shot the upstream profiles start evolving moving towards flatter profiles as the density is raised. Similar observations can be done for shot # 34281 where upstream profile evolution starts whenever the outer divertor moves to the high-recycling regime whereas for the shot with lower divertor neutral pressure the profile remains substantially unmodified without any signature of target ion flux roll-over.

Inter-ELM filament characteristics have been investigated in these shots. Determination of inter-ELM intervals were done in analogy to [15]. The results concerning the relation with inter-ELM density profile flattening are summarized in Figure 21 where the e-folding length is shown as a function of divertor collisionality Λ_{div} in panels (a) and (c) and as a function of inter-ELM blob-size in panels (b) and (d). The fluctuation data, as well as the corresponding λ_n, has been obtained at $\rho \approx 1.05$, further away from the separatrix with respect to the data in L-Mode. The symbol colour code is proportional to the divertor neutral pressure as measured in the sub-divertor area in panel (a) and (b), and to the midplane neutral pressure as measured from midplane gauges in panel (c) and (d). For completeness, since the local ion and electron temperature were not available for these shots at the probe location for a proper computation of ρ_s, we have assumed that $T_e = 15$ eV and $T_i = 45$ eV for $\Lambda_{div} \lesssim 1$ and $T_e = T_i = 15$ eV for higher collisionality in accordance to the observation reported in [10]. We are aware of the possible uncertainties caused by the lack of information on the ion temperature but as pointed out in [53, 10] better comparison between experimental results and theoretical predictions are observed whenever hot ion approximation is retained: this motivates our choice in the determination of ion sound gyroradius. From this analysis we can recognize the relation suggested in [7]

with increasing λ_n observed when crossing $\Lambda_{div} \approx 1$ even though, as anticipated in [15], the transition is smoother and less clear than in L-Mode. Larger values of λ_n are obtained at higher neutral pressures (both divertor and midplane), consistently with the constant increase of pressure during the fuelling ramp observed in Figure 18. On the other hand, from panel (d) of Figure 21 we recognize that large blobs are insufficient to ensure the increase of λ_n but for the same blob-size flatter profiles are obtained only for higher values of neutrals at the midplane. Also the relation between e-folding length and blob-size is weaker than in L-Mode thus supporting the idea that the paradigm of filamentary regime transition proposed for the L-Mode needs to be revised to provide unified description of the L and H-mode dynamics.

To corroborate the measurements of blob properties performed by probes, we used gas-puff-imaging (GPI) in the same discharges. The GPI system on AUG introduces a local density of neutrals via a piezoelectric valve at the LFS radius $R = 2.19\,\mathrm{m}$ and height $z = -0.16\,\mathrm{m}$ [59]. In the experiments reported, a He puff was used to enhance line emission and allow toroidal localization of fluctuation signals, and the brightest, 587.6nm wavelength line of helium was imaged using a Phantom v711 camera sampled at 398kHz. Figure 22 compares results of the GPI measurements in shots #34276 and 34278 (without and with cryogenic pump) based on a cross-correlation over 1 ms of signal, with zero time lag, using a reference at $\rho \simeq 1.05$. The solid black line indicates the contour line at 0.5 correlation value. Since the fluctuation power in the far SOL is dominated by filaments, the correlation is a good proxy to an average blob shape, i.e. filament cross-section. However, since the measurements were performed in H-modes, in the time histories used for cross-correlation care was taken to avoid ELM bursts, which overwhelm blob filaments by orders of magnitude. Both patterns show a somewhat radially elongated structure, with poloidal and radial correlation lengths, estimated as half of the FWHM value of the correlation, $\Lambda_\theta(34276) = 0.5\,\mathrm{cm}$, $\Lambda_\theta(34278) = 0.75\,\mathrm{cm}$ and $\Lambda_r(both) = 1.2\,\mathrm{cm}$ respectively.

Poloidal and radial velocities are extracted from the motion of emission features using a tracking TDE (time delay estimation) method [60], suitable for systems with a high degree of spatial resolution with relatively slow time resolution and detection speeds. Direct velocimetry results are converted to nominal minor radius and poloidal directions using the equilibrium reconstruction. At the marked far SOL location of $\rho = 1.05$ filament velocities in #34276 are $v_\theta = 330 \pm 30\,\mathrm{m/s}$, $v_r = 220 \pm 120\,\mathrm{m/s}$ and in # 34278 $v_\theta = 310 \pm 30\,\mathrm{m/s}$, $v_r = 120 \pm 80\,\mathrm{m/s}$. In the above, velocimetry errors are estimated as the larger one of the fit error in tracking or the deviation between instances of inter-ELM activity.

Since the gas puffing and the probe plunges were not synchronized a one to one comparison is not possible given also the non stationary condition of the discharge. Nevertheless, with similar conditions the probe estimates are respectively $\delta_b = 0.9\,\mathrm{cm}$ and $\delta_b = 1.1\,\mathrm{cm}$, thus compatible with the GPI estimate. Also the velocity estimates are consistent with a radial and poloidal velocity of $v_r = 450$, $v_\theta = 160$ m/s for # 34276 and $v_r = 250$, $v_\theta = 260$ for # 34278. Given the different location and type of measurement

this represents an excellent agreement providing confidence in the observations carried out by insertable probe measurement.

5. Conclusion

A unified effort within the EUROfusion Medium-Size-Tokamaks (MST1) Work programme has been coordinated to explore the role of filamentary transport in high density tokamak regimes both in L and H-mode, particular focusing on the issue of *SOL shoulder formation*. Comparable current scans at constant toroidal field or constant q_{95} have been performed to disentangle the role of plasma current from the modification of parallel connection length. On AUG we have proved that the shoulder formation at different current behavior, with or without constant $L_{\parallel}$, is well reconciled in terms of edge Greenwald fraction. On TCV this is true only for the two lower current levels explored in the constant toroidal field scan. Furthermore, in analogy with JET, upstream profile starts evolving with the transition to a high recycling regime for AUG, and is associated with an enhancement of D_{α} radiation in the LFS SOL region, as reported in [38] for JET Horizontal Target plasmas. On the other hand TCV, with its completely open divertor, exhibits a different divertor dynamical behaviour, with the target density increasing almost linearly with fuelling: for both the devices we have proved that the evolution of the upstream profiles follows the dynamics of the divertor, with more pronounced and flatter profiles obtained after target density roll-over. The lack of detachment at lower currents observed in TCV during the constant q_{95} scan prevents upstream variation and the development of a SOL density profile shoulder. In L-Mode plasmas, the density e-folding length increases with blob-size independently of the current in all scans performed on ASDEX Upgrade, whereas the same relation, even if recognizable in the scan at constant toroidal field, is weaker and more scattered for TCV. What has been proved clearly is that the blob-size for both devices increases with the edge Greenwald normalized density, and at least for AUG, larger filaments are observed at higher neutral pressure (the dependence on the midplane neutral pressure is more robust and clear as seen in Figure 19 (d)). The filamentary characteristics in L-Mode have been considered in the framework of the 2-region model, which allows the distinction between connected and disconnected regime. We have shown that for AUG the points at lower collisionality are compatible with electrically connected filaments whereas the transition to disconnected regimes is obtained at larger collisionality. Differently filaments in TCV appear to be always in disconnected regimes, confirming previous analysis [27]. Work is in progress to understand if this difference could be at the basis of the different behavior with respect to divertor collisionality observed in the two devices. More detailed investigations are in any case mandatory in this case due to the uncertainty in the estimate of the local ion and electron temperature under the different conditions. H-Mode density shoulders have been obtained in ASDEX Upgrade, in discharges with high levels of both fuelling and seeding. We have demonstrated that neither large divertor collisionality nor large blobs are sufficient on themselves to guarantee the shoulder

formation, but that a high neutral density, in particular in the midplane region, is mandatory. The reason why this is not confirmed in other devices [8] is presently under investigation. Work is presently in progress to extend the H-Mode analysis in TCV, where high density H-Mode in detachment conditions has not yet been achieved even with high values of inter-ELM divertor collisionality.

Acknowledgments

This work has been carried out within the framework of the EUROfusion Consortium and has received funding from the Euratom research and training programme 2014-2018 and 2019-2020 under grant agreement No 633053. The views and opinions expressed herein do not necessarily reflect those of the European Commission. This work was supported in part by the Swiss National Science Foundation and the CEEPUS network AT-0063. This work was supported in part by the US Department of Energy under Award Number DE-SC0010529.

References

[1] Kočan M, Pitts R A, Arnoux G, Balboa I, de Vries P C, Dejarnac R, Furno I, Goldston R J, Gribov Y, Horaček J, Komm M, Labit B, LaBombard B, Lasnier C J, Mitteau R, Nespoli F, Pace D, Panek R, Stangeby P C, Terry J L, Tsui C and Vondracek P 2015 *Nucl. Fus.* **55** 033019

[2] McCormick K, Kyriakakis G, Neuhauser J, Kakoulidis E, Schweinzer J and Tsois N 1992 *Journal of Nuclear Materials* **196** 264–270

[3] Asakura N, Koide Y, Itami K, Hosogane N, Shimizu K, Tsuji-Iio S, Sakurai S and Sakasai A 1997 *Journal of Nuclear Materials* **241-243** 559–563

[4] LaBombard B, Boivin R L, Greenwald M, Hughes J, Lipschultz B, Mossessian D, Pitcher C S, Terry J L, Zweben S J and Group A 2001 *Phys. Plasmas* **8** 2107

[5] Rudakov D L, Boedo J A, Moyer R A, Stangeby P C, Watkins J G, Whyte D G, Zeng L, Brooks N H, Doerner R P, Evans T E, Fenstermacher M E, Groth M, Hollmann E M, Krasheninnikov S I, Lasnier C J, Leonard A W, Mahdavi M A, McKee G R, McLean A G, Pigarov A Y, Wampler W R, Wang G, West W P and Wong C P C 2005 *Nuclear Fusion* **45** 1589–1599

[6] Garcia O E, Pitts R A, Horaček J, Madsen J, Naulin V, Nielsen A H and Rasmussen J J 2007 *Plasma Phys. Contr. Fus.* **49** B47

[7] Carralero D, Manz P, Aho-Mantila L, Birkenmeier G, Brix M, Groth M, Müller H W, Stroth U, Vianello N, Wolfrum E, ASDEX Upgrade Team, JET Contributors and EUROfusion MST1 Team 2015 *Phys. Rev. Lett.* **115** 215002

[8] Militello F, Garzotti L, Harrison J, Omotani J T, Scannell R, Allan S, Kirk A, Lupelli I, Thornton A J and team t M 2016 *Nucl. Fusion* **56** 016006

[9] Vianello N, Tsui C K W K W, Theiler C, Allan S, Boedo J A, Labit B, Reimerdes H, Verhaegh K, Vijvers W A J, Walkden N, Costea S, Kovačič J, Ionita C, Naulin V, Nielsen A, Rasmussen J J, Schneider B S, Schrittwieser R, Spolaore M, Carralero D, Madsen J, Lipschultz B and Militello F 2017 *Nucl. Fusion* **57** 116014

[10] Carralero D, Artene S, Bernert M, Birkenmeier G, Faitsch M, Manz P, de Marne P, Stroth U, Wischmeier M and Wolfrum E 2018 *Nuclear Fusion* **58** 096015

[11] LaBombard B, Goetz J A, Hutchinson I, Jablonski D, Kesner J, Kurz C, Lipschultz B, McCracken G M, Niemczewski A, Terry J, Allen A, Boivin R L, Bombarda F, Bonoli P, Christensen C, Fiore C, Garnier D, Golovato S, Granetz R, Greenwald M, Horne S, Hubbard A, Irby J, Lo D, Lumma D, Marmar E, May M, Mazurenko A, Nachtrieb R, Ohkawa H, O'Shea P, Porkolab M, Reardon J, Rice J, Rost J, Schachter J, Snipes J, Sorci J, Stek P, Takase Y, Wang Y, Watterson R, Weaver J, Welch B and Wolfe S 1997 *Journal of Nuclear Materials* **241-243** 149–166

[12] Boedo J A, Rudakov D, Moyer R, Krasheninnikov S, Whyte D, McKee G, Tynan G, Schaffer M, Stangeby P, West P, Allen S, Evans T, Fonck R, Hollmann E, Leonard A, Mahdavi A, Porter G, Tillack M and Antar G 2001 *Physics of Plasmas* **8** 4826–4833

[13] Lipschultz B, LaBombard B, Pitcher C S and Boivin R 2002 *Plasma Physics and Controlled Fusion* **44** 733–748

[14] Müller H W, Bernert M, Carralero D, Kallenbach A, Kurzan B, Scarabosio A, Sieglin B, Tophøj L, Vianello N and Wolfrum E 2015 *Journ of Nucl. Mater.* **463** 739–743

[15] Carralero D, Siccinio M, Komm M, Artene S A, D'Isa F A, Adamek J, Aho-Mantila L, Birkenmeier G, Brix M, Fuchert G, Groth M, Lunt T, Manz P, Madsen J, Marsen S, Müller H W, Stroth U, Sun H J, Vianello N, Wischmeier M, Wolfrum E, Team A U, Team C, Contributors J and Team T E M 2017 *Nucl. Fusion* **57** 056044

[16] Bernert M, Eich T, Kallenbach A, Carralero D, Huber A, Lang P, Potzel S, Reimold F, Schweinzer J, Viezzer E *et al.* 2014 *Plasma Phys. Control. Fus.* **57** 014038

[17] Eich T, Goldston R J, Kallenbach A, Sieglin B, Sun H J, Team A U and Contributors J 2018 *Nuclear Fusion* **58** 034001

[18] Kallenbach A, Adamek J, Aho-Mantila L, Äkäslompolo S, Angioni C, Atanasiu C, Balden M, Behler K, Belonohy E, Bergmann A, Bernert M, Bilato R, Bobkov V, Boom J, Bottino A,

Braun F, Brüdgam M, Buhler A, Burckhart A, Chankin A, Classen I, Conway G, Coster D, de Marné P, D'Inca R, Drube R, Dux R, Eich T, Endstrasser N, Engelhardt K, Esposito B, Fable E, Fahrbach H U, Fattorini L, Fischer R, Flaws A, Fünfgelder H, Fuchs J, Gál K, Muñoz M G, Geiger B, Adamov M G, Giannone L, Giroud C, Görler T, da Graca S, Greuner H, Gruber O, Gude A, Günter S, Haas G, Hakola A, Hangan D, Happel T, Hauff T, Heinemann B, Herrmann A, Hicks N, Hobirk J, Höhnle H, Hölzl M, Hopf C, Horton L, Huart M, Igochine V, Ionita C, Janzer A, Jenko F, Käsemann C P, Kálvin S, Kardaun O, Kaufmann M, Kirk A, Klingshirn H J, Kocan M, Kocsis G, Kollotzek H, Konz C, Koslowski R, Krieger K, Kurki-Suonio T, Kurzan B, Lackner K, Lang P, Lauber P, Laux M, Leipold F, Leuterer F, Lohs A, Jr N L, Lunt T, Lyssoivan A, Maier H, Maggi C, Mank K, Manso M E, Maraschek M, Martin P, Mayer M, McCarthy P, McDermott R, Meister H, Menchero L, Meo F, Merkel P, Merkel R, Mertens V, Merz F, Mlynek A, Monaco F, Müller H, Münich M, Murmann H, Neu G, Neu R, Nold B, Noterdaeme J M, Park H, Pautasso G, Pereverzev G, Podoba Y, Pompon F, Poli E, Polochiy K, Potzel S, Prechtl M, Püschel M, Pütterich T, Rathgeber S, Raupp G, Reich M, Reiter B, Ribeiro T, Riedl R, Rohde V, Roth J, Rott M, Ryter F, Sandmann W, Santos J, Sassenberg K, Sauter P, Scarabosio A, Schall G, Schmid K, Schneider P, Schneider W, Schramm G, Schrittwieser R, Schweinzer J, Scott B, Sempf M, Serra F, Sertoli M, Siccinio M, Sigalov A, Silva A, Sips A, Sommer F, Stäbler A, Stober J, Streibl B, Strumberger E, Sugiyama K, Suttrop W, Szepesi T, Tardini G, Tichmann C, Told D, Treutterer W, Urso L, Varela P, Vincente J, Vianello N, Vierle T, Viezzer E, Vorpahl C, Wagner D, Weller A, Wenninger R, Wieland B, Wigger C, Willensdorfer M, Wischmeier M, Wolfrum E, Würsching E, Yadikin D, Yu Q, Zammuto I, Zasche D, Zehetbauer T, Zhang Y, Zilker M and Zohm H 2011 *Nuclear Fusion* **51** 094012 URL http://stacks.iop.org/0029-5515/51/i=9/a=094012

[19] Willensdorfer M, Birkenmeier G, Fischer R, Laggner F M, Wolfrum E, Veres G, Aumayr F, Carralero D, Guimar?is L, Kurzan B and Team t A U 2014 *Plasma Physics and Controlled Fusion* **56** 025008

[20] Fischer R, Wolfrum E, Schweinzer J and Team t A U 2008 *Plasma Physics and Controlled Fusion* **50** 085009

[21] Carralero D, Birkenmeier G, Müller H W, Manz P, deMarne P, Müller S H, Reimold F, Stroth U, Wischmeier M, Wolfrum E and Team t A U 2014 *Nuclear Fusion* **54** 123005

[22] Coda S, Ahn J, Albanese R, Alberti S, Alessi E, Allan S, Anand H, Anastassiou G, Andrèbe Y, Angioni C, Ariola M, Bernert M, Beurskens M, Bin W, Blanchard P, Blanken T, Boedo J, Bolzonella T, Bouquey F, Braunmüller F, Bufferand H, Buratti P, Calabró G, Camenen Y, Carnevale D, Carpanese F, Causa F, Cesario R, Chapman I, Chellai O, Choi D, Cianfarani C, Ciraolo G, Citrin J, Costea S, Crisanti F, Cruz N, Czarnecka A, Decker J, Masi G D, Tommasi G D, Douai D, Dunne M, Duval B, Eich T, Elmore S, Esposito B, Faitsch M, Fasoli A, Fedorczak N, Felici F, Février O, Ficker O, Fietz S, Fontana M, Frassinetti L, Furno I, Galeani S, Gallo A, Galperti C, Garavaglia S, Garrido I, Geiger B, Giovannozzi E, Gobbin M, Goodman T, Gorini G, Gospodarczyk M, Granucci G, Graves J, Guirlet R, Hakola A, Ham C, Harrison J, Hawke J, Hennequin P, Hnat B, Hogeweij D, Hogge J P, Honoré C, Hopf C, Horáček J, Huang Z, Igochine V, Innocente P, Schrittwieser C I, Isliker H, Jacquier R, Jardin A, Kamleitner J, Karpushov A, Keeling D, Kirneva N, Kong M, Koubiti M, Kovacic J, Krämer-Flecken A, Krawczyk N, Kudlacek O, Labit B, Lazzaro E, Le H, Lipschultz B, Llobet X, Lomanowski B, Loschiavo V, Lunt T, Maget P, Maljaars E, Malygin A, Maraschek M, Marini C, Martin P, Martin Y, Mastrostefano S, Maurizio R, Mavridis M, Mazon D, McAdams R, McDermott R, Merle A, Meyer H, Militello F, Miron I, Cabrera P M, Moret J M, Moro A, Moulton D, Naulin V, Nespoli F, Nielsen A, Nocente M, Nouailletas R, Nowak S, Odstrčil T, Papp G, Papřok R, Pau A, Pautasso G, Ridolfini V P, Piovesan P, Piron C, Pisokas T, Porte L, Preynas M, Ramogida G, Rapson C, Rasmussen J J, Reich M, Reimerdes H, Reux C, Ricci P, Rittich D, Riva F, Robinson T, Saarelma S, Saint-Laurent F, Sauter O, Scannell R, Schlatter C, Schneider B, Schneider P, Schrittwieser R, Sciortino F, Sertoli M, Sheikh U, Sieglin B, Silva M, Sinha J,

Sozzi C, Spolaore M, Stange T, Stoltzfus-Dueck T, Tamain P, Teplukhina A, Testa D, Theiler C, Thornton A, Tophøj L, Tran M, Tsironis C, Tsui C, Uccello A, Vartanian S, Verdoolaege G, Verhaegh K, Vermare L, Vianello N, Vijvers W, Vlahos L, Vu N, Walkden N, Wauters T, Weisen H, Wischmeier M, Zestanakis P, Zuin M and team t E M 2017 *Nuclear Fusion* **57** 102011

[23] Verhaegh K, Lipschultz B, Duval B P, Harrison J R, Reimerdes H, Theiler C, Labit B, Maurizio R, Marini C, Nespoli F, Sheikh U, Tsui C K, Vianello N and Vijvers W A J 2017 *Nuclear Materials and Energy* **12** 1112–1117

[24] Furno I, Weisen H, Mlynar J, Pitts R A, Llobet X, Marmillod P and Pochon G P 1999 *Review of Scientific Instruments* **70**

[25] Février O, Theiler C, Oliveira H D, Labit B, Fedorczak N and Baillod A 2018 *Review of Scientific Instruments* **89** 053502 URL https://aip.scitation.org/doi/10.1063/1.5022459

[26] Boedo J 2009 *Journal of Nuclear Materials* **390** 29

[27] Tsui C K, Boedo J A, Myra J R, Duval B, Labit B, Theiler C, Vianello N, Vijvers W A J, Reimerdes H, Coda S, Février O, Harrison J R, Horaček J, Lipschultz B, Maurizio R, Nespoli F, Sheikh U, Verhaegh K, Walkden N, TCV Team and Team E M 2018 *Physics of Plasmas* **25** 072506

[28] Ho A, Citrin J, Auriemma F, Bourdelle C, Casson F J, Kim H T, Manas P, Szepesi G, Weisen H and Contributors J 2019 *Nuclear Fusion* **59** 056007

[29] Pucella G, Tudisco O, Apicella M L, Apruzzese G, Artaserse G, Belli F, Bin W, Boncagni L, Botrugno A, Buratti P, Calabrò G, Castaldo C, Cianfarani C, Cocilovo V, Dimatteo L, Esposito B, Frigione D, Gabellieri L, Giovannozzi E, Granucci G, Marinucci M, Marocco D, Martines E, Mazzitelli G, Mazzotta C, Nowak S, Ramogida G, Romano A, Tuccillo A A, Zeng L and Zuin M 2013 *Nuclear Fusion* **53** 083002

[30] Theiler C, Lipschultz B, Harrison J, Labit B, Reimerdes H, Tsui C, Vijvers W, Boedo J, Duval B, Elmore S *et al.* 2017 *Nuclear Fusion* **57** 072008

[31] Sang C, Stangeby P, Guo H, Leonard A, Covele B, Lao L, Moser A and Thomas D 2016 *Plasma Physics and Controlled Fusion* **59** 025009

[32] Pitts R, Duval B, Loarte A, Moret J M, Boedo J, Coster D, Furno I, Horacek J, Kukushkin A, Reiter D, Rommers J and Team T T 2001 *Journal of Nuclear Materials* **290** 940–946

[33] Park J S, Groth M, Pitts R, Bak J G, Thatipamula S G, Juhn J W, Hong S H and Choe W *Nuclear Fusion* **58** 126033

[34] Fil A, Dudson B, Lipschultz B, Moulton D, Verhaegh K, Février O and Wensing M 2018 *Contributions to Plasma Physics* **47** S203

[35] Myra J R, Russell D A and D'Ippolito D A 2006 *Physics of Plasmas* **13** 112502

[36] Fevrier O, Theiler C, Tsui C and Labit B 2019 *to be submitted to Plasma Physics and Controlled Fusion*

[37] Militello F and Omotani J T 2016 *Nuclear Fusion* **56** 104004

[38] Wynn A, Lipschultz B, Cziegler I, Harrison J, Jaervinen A, Matthews G F, Schmitz J, Tal B, Brix M, Guillemaut C, Frigione D, Huber A, Joffrin E, Kruzei U, Militello F, Nielsen A, Walkden N R, Wiesen S and Contributors J 2018 *Nuclear Fusion* **58** 056001

[39] Harhausen J, Kallenbach A, Fuchs C and Team t A U 2011 *Plasma Physics and Controlled Fusion* **53** 025002

[40] Carr M, Meakins A, Bernert M, David P, Giroud C, Harrison J, Henderson S, Lipschultz B, Reimold F, Team E M and Team A U 2018 *The Review of scientific instruments* **89** 083506

[41] Andersen A 1984 *Ultrasonic Imaging* **6** 81–94

[42] Agostini M, Brombin M, Serianni G and Pasqualotto R 2011 *Physical Review Special Topics - Accelerators and Beams* **14** 102801

[43] Reimold F, Wischmeier M, Potzel S, Guimarãis L, Reiter D, Bernert M, Dunne M and Lunt T 2017 *Nuclear Materials and Energy* **12** 193–199

[44] Potzel S, Wischmeier M, Bernert M, Dux R, Reimold F, Scarabosio A, Brezinsek S, Clever M, Huber A, Meigs A and Stamp M 2015 *Journal of Nuclear Materials* **463** 541–545

[45] Agostini M, Vianello N, Carraro L, Cavedon M, Carralero D, Dux R, Lunt T, Naulin V, Spolaore M and Wolfrum E 2019 *accepted Plasma Physics and Controlled Fusion*

[46] Boedo J A, Myra J R, Zweben S, Maingi R, Maqueda R J, Soukhanovskii V A, Ahn J W, Canik J, Crocker N, D'Ippolito D A, Bell R, Kugel H, Leblanc B, Roquemore L A, Rudakov D L and Team N 2014 *Physics of Plasmas (1994-present)* **21** 042309

[47] Garcia O E, Horaček J, Pitts R A, Nielsen A H, Fundamenski W, Naulin V and Rasmussen J J 2007 *Nuclear Fusion* **47** 667 676

[48] Garcia O E, Fritzner S M, Kube R, Cziegler I, LaBombard B and Terry J L 2013 *Physics of Plasmas* **20** 055901

[49] Theodorsen A, Garcia O E, Horacek J, Kube R and Pitts R A 2016 *Plasma Physics and Controlled Fusion* **58** 044006

[50] Carralero D, Madsen J, Artene S, Bernert M, Birkenmeier G, Eich T, Fuchert G, Laggner F, Naulin V, Manz P, Vianello N, Wolfrum E, team t E M and Team t A U 2017 *Nuclear Materials and Energy* **12** 1189–1193

[51] Birkenmeier G, Laggner F M, Willensdorfer M, Kobayashi T, Manz P, Wolfrum E, Carralero D, Fischer R, Sieglin B, Fuchert G, Stroth U and team t A u 2014 *Plasma Physics and Controlled Fusion* **56** 075019

[52] Fuchert G, Birkenmeier G, Carralero D, Lunt T, Manz P, Müller H W, Nold B, Ramisch M, Rohde V and Stroth U 2014 *Plasma Physics and Controlled Fusion* **56** 125001

[53] Birkenmeier G, Manz P, Carralero D, Laggner F M, Fuchert G, Krieger K, Maier H, Reimold F, Schmid K, Dux R, Pütterich T, Willensdorfer M, Wolfrum E and Team T A U 2015 *Nuclear Fusion* **55** 033018

[54] Wersal C and Ricci P 2015 *Nuclear Fusion* **55** 123014

[55] Thrysøe A S, Tophøj L E H, Naulin V, Rasmussen J J, Madsen J and Nielsen A H 2016 *Plasma Physics and Controlled Fusion* **58** 044010

[56] Thrysøe A S, Løiten M, Madsen J, Naulin V, Nielsen A H and Rasmussen J J 2018 *Physics of Plasmas* **25** 032307

[57] Thrysøe A S, Madsen J, Naulin V and Rasmussen J J 2018 *Nuclear Fusion* **58** 096005

[58] Sun H J, Wolfrum E, Eich T, Kurzan B, Kallenbach A, Happel T and Stroth U *Plasma Physics and Controlled Fusion* **61** 014005

[59] Griener M, Wolfrum E, Cavedon M, Dux R, Rohde V, Sochor M, Burgos J M M, Schmitz O, Stroth U and Team A U *Review of Scientific Instruments* **89** 10D102

[60] Zweben S J, Terry J L, Agostini M, Davis W M, Diallo A, Ellis R A, Golfinopoulos T, Grulke O, Hughes J W, LaBombard B, Landreman M, Myra J R, Pace D C and Stotler D P *Physics of Plasmas* **20** 072503

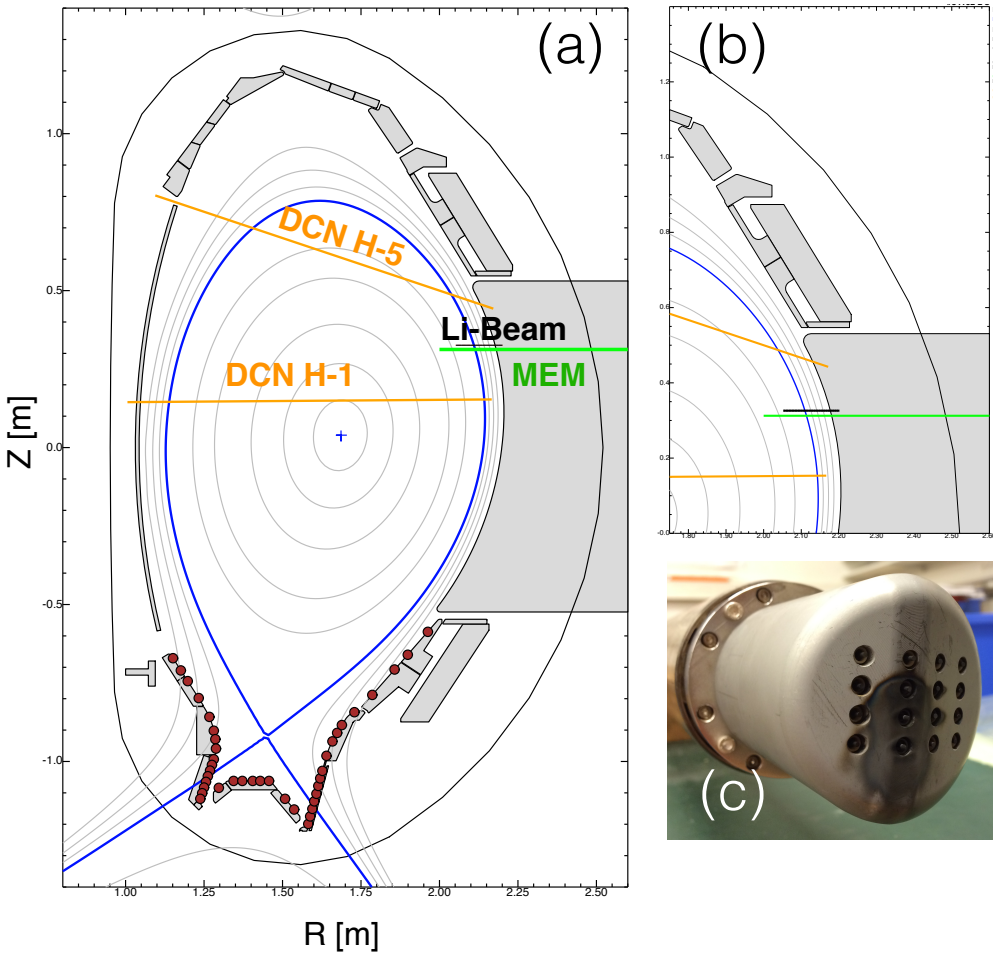

Figure 1: Experimental layout on ASDEX Upgrade. (a) Poloidal section of the typical L-mode discharge performed in the so called EOC shape. The separatrix is indicated in blue line, whereas the position of the principal diagnostics are indicated. In particular the position of the Li-Beam (black line), the Midplane manipulator (green line), the edge and core interferometer chords (orange lines) and the Langmuir probe measurements are shown. In panel (b) a zoom of the field line close to the location of the measurements whereas on panel (c) a photo of the probe head used as seen from the plasma.

Figures

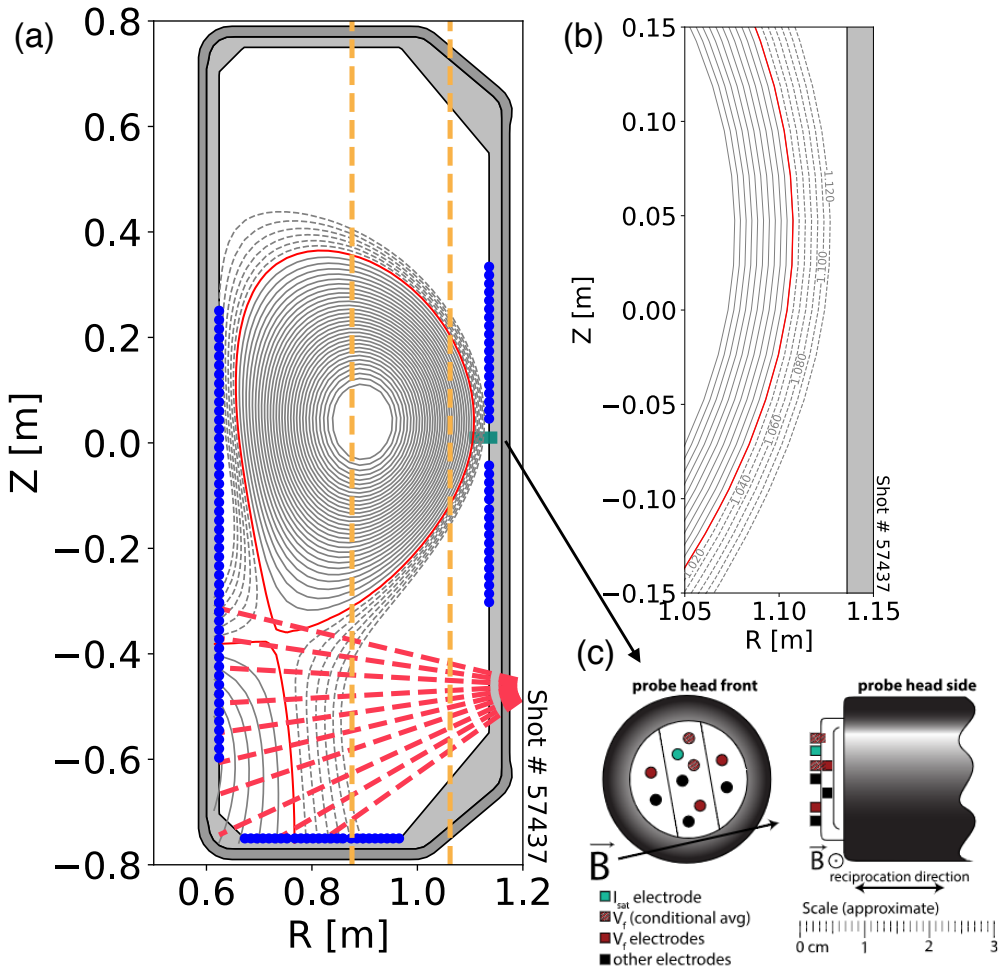

Figure 2: (a) Poloidal cross-section of TCV tokamak with a typical equilibrium from one of the shot used in the present paper. The LoS of bolometry (reddish) and Far Infrared Interferometer (orange) are shown as well as the location of the embedded Langmuir Probes (blue) and the position of the midplane fast reciprocating manipulator (green). (b) Zoom of the edge and SOL region around the midplane (c) Scheme of the Fast Reciprocating probe used.

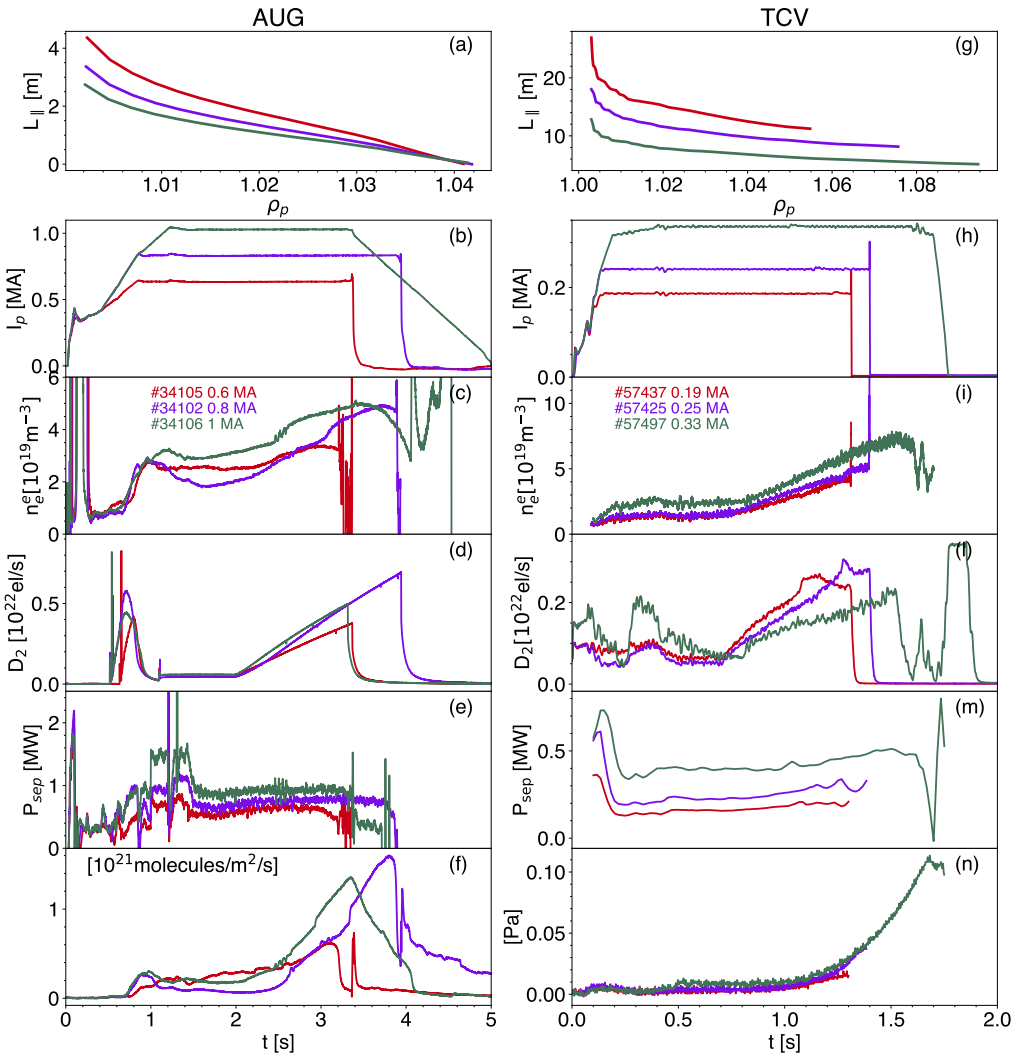

Figure 3: Discharge parameters for AUG (left columns) and TCV (right columns) for current scans analysis performed at constant B_t. From top to bottom: (a) and (g) parallel connection length $L_{||}$ from target to X-point heights for 3 discharges at different current levels but same toroidal field. Toroidal plasma current (b) and (h), edge line average density (c) and (i), total deuterium fueling (d) and (l), Power crossing the separatrix (e) and (m), divertor pressure (f) and (n).

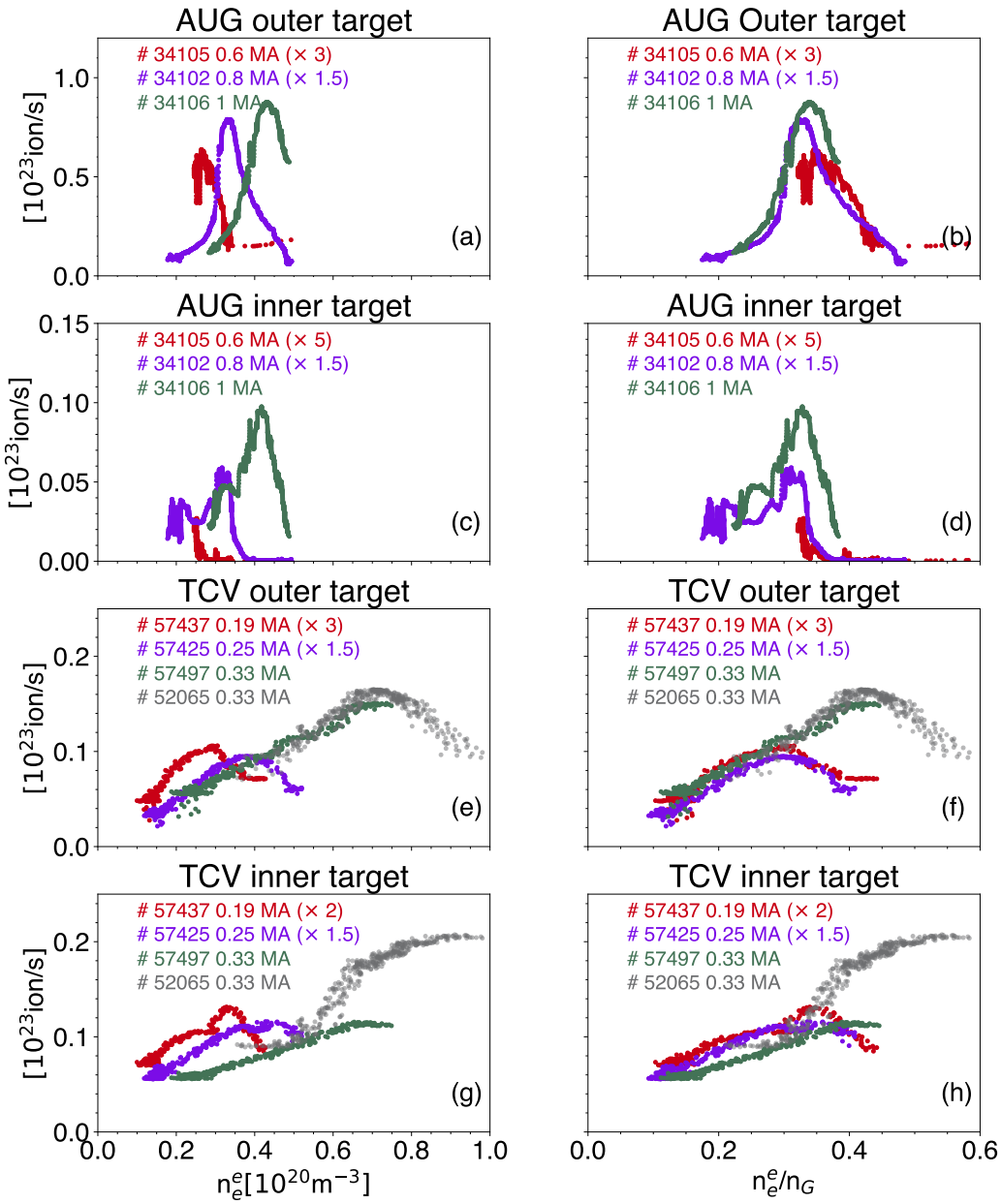

Figure 4: Outer Target profiles as a function of edge density (a) and edge density normalized to Greenwald fraction (b) for AUG. Inner Target profiles as a function of edge density (c) and edge density normalized to Greenwald fraction (d) for AUG. Outer Target profiles as a function of edge density (e) and edge density normalized to Greenwald fraction (f) for TCV. Inner Target profiles as a function of edge density (g) and edge density normalized to Greenwald fraction (h) for TCV. All the data refer to the scan at constant toroidal field.

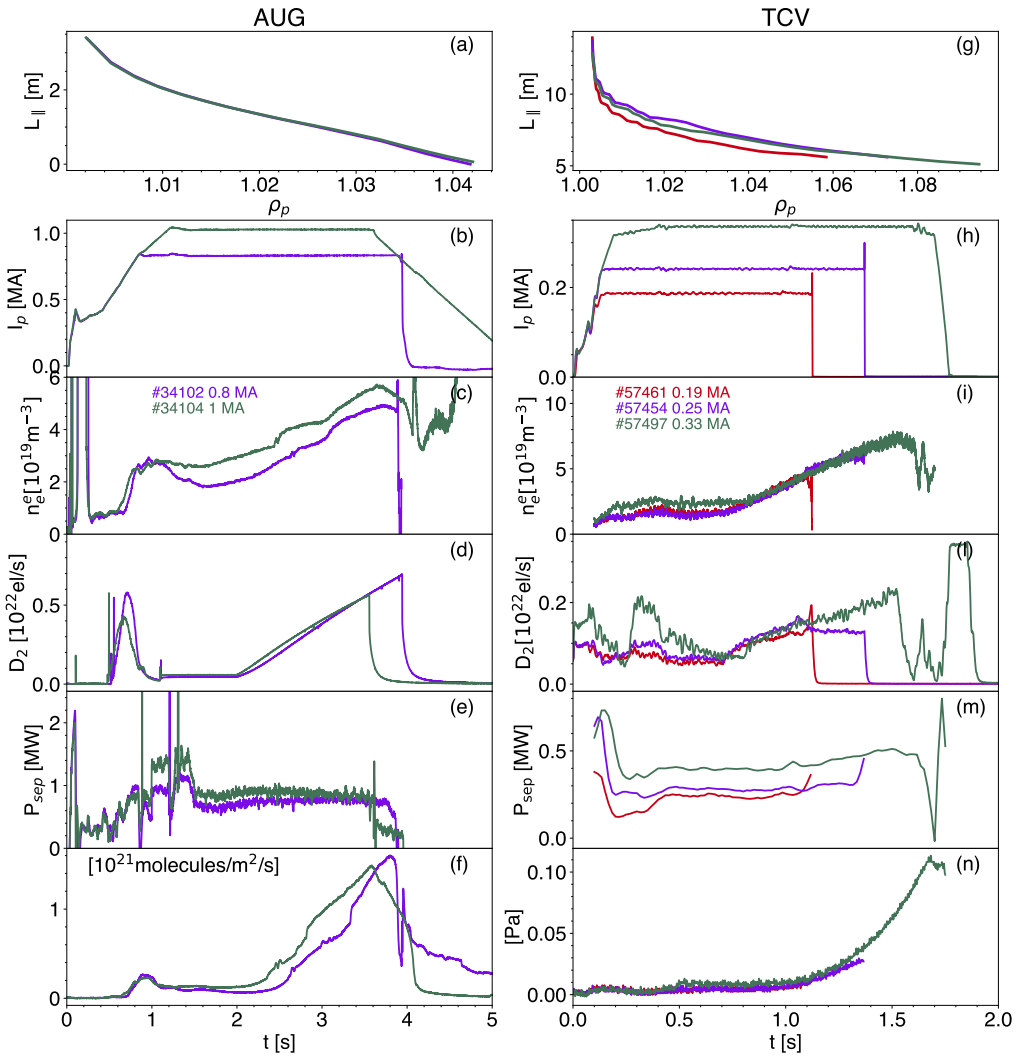

Figure 5: Discharge parameters for AUG (left columns) and TCV (right columns) for current scans analysis performed at constant q_{95}. From top to bottom: (a) and (g) parallel connection length $L_\parallel$ from target to X-point heights for 3 discharges at different current levels but same toroidal field. Toroidal plasma current (b) and (h), edge line average density (c) and (i), total deuterium fueling (d) and (l), Power crossing the separatrix (e) and (m), divertor pressure (f) and (n).

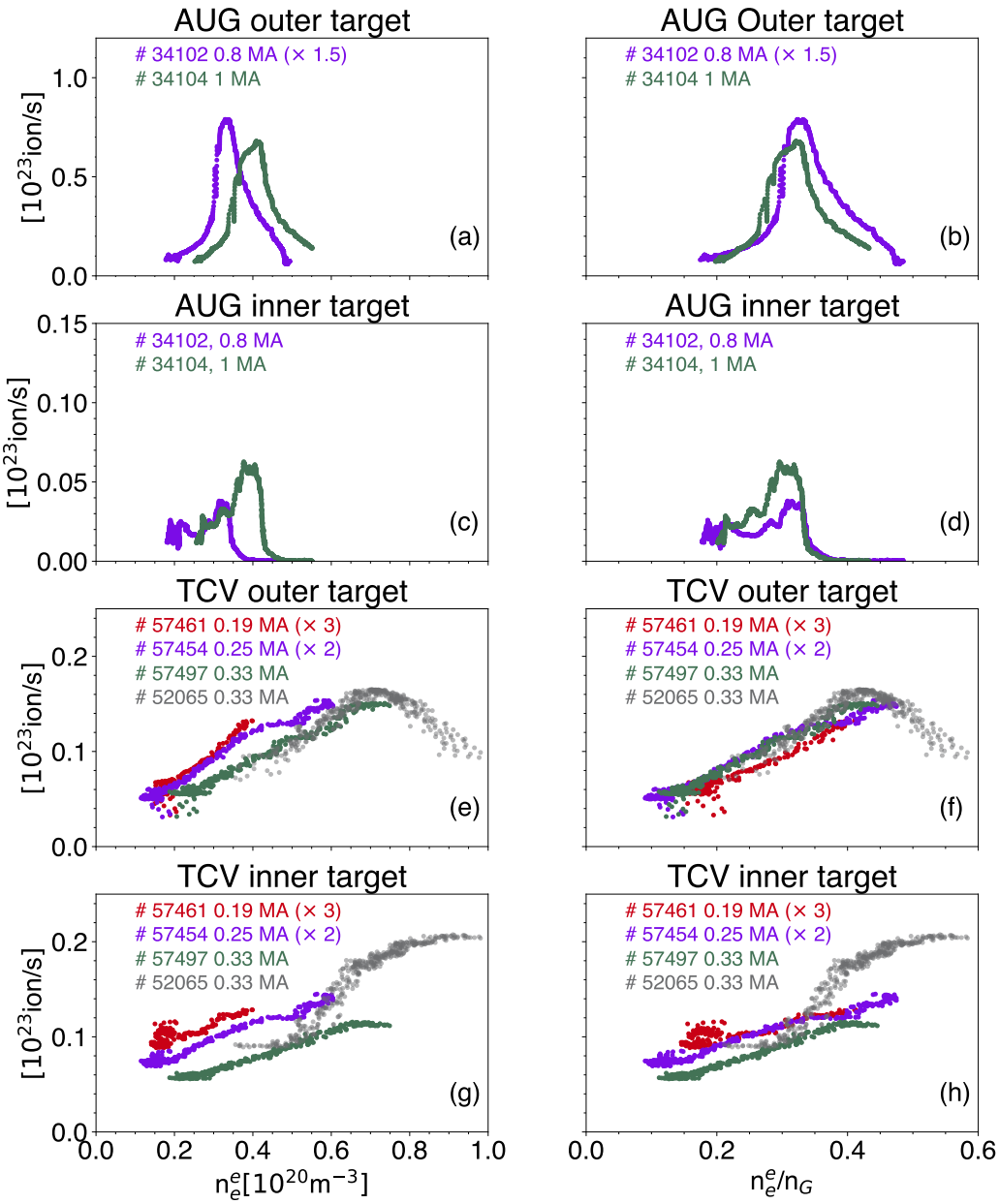

Figure 6: Outer Target profiles as a function of edge density (a) and edge density normalized to Greenwald fraction (b) for AUG. Inner Target profiles as a function of edge density (c) and edge density normalized to Greenwald fraction (d) for AUG. Outer Target profiles as a function of edge density (e) and edge density normalized to Greenwald fraction (f) for TCV. Inner Target profiles as a function of edge density (g) and edge density normalized to Greenwald fraction (h) for TCV. All the data refer to the scan at constant q_{95}.

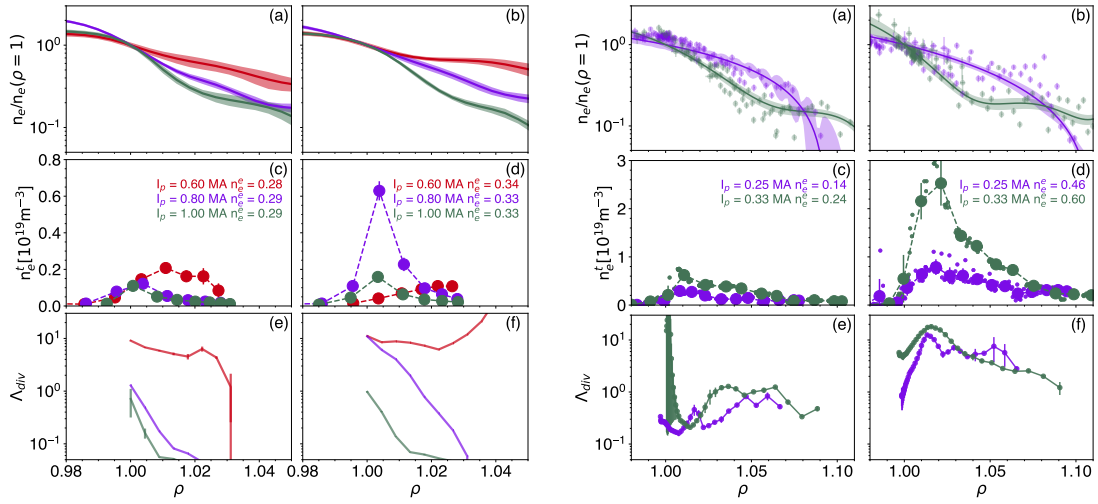

(i) ASDEX Upgrade (ii) TCV

Figure 7: (a) and (b) Upstream density profiles, normalized to the values at the separatrix at three different currents (colour code) with the same B_t at the same level of Edge density. For TCV both the raw data and the Gaussian process regression fits are shown (c) and (d) Outer target density profiles as a function of normalized poloidal flux ρ. The large circles and corresponding error bars are the results of a binning procedure on raw data. (e) and (f) Divertor collisionality as a function of ρ. The Λ profiles error are obtained propagating the errors on density and temperature. Sub-figure (i) refers to AUG whereas sub-figure (ii) refers to TCV.

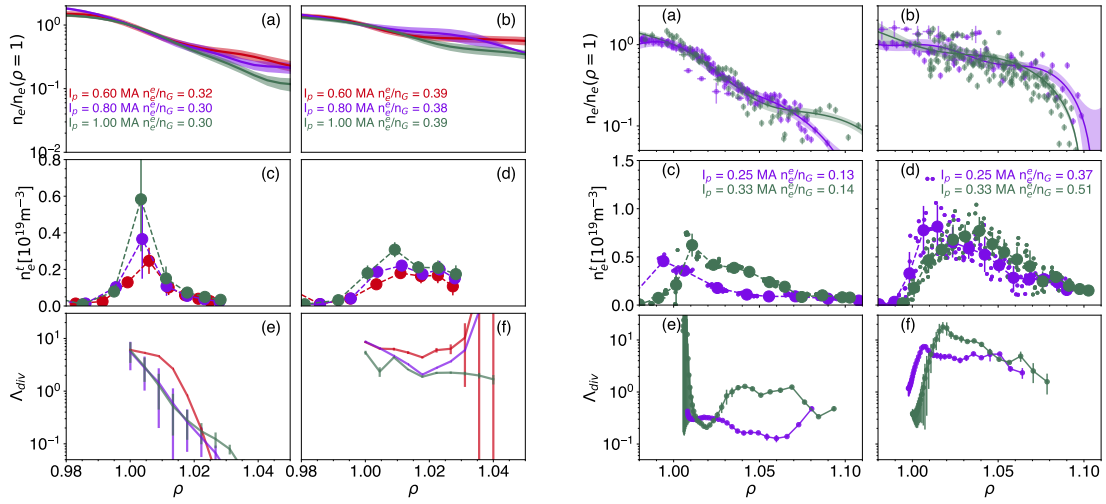

(i) ASDEX Upgrade (ii) TCV

Figure 8: (a) and (b) Upstream density profiles, normalized to the values at the separatrix at different currents (colour code) with the same B_t at the same level of edge Greenwald fraction. For TCV both the raw data and the Gaussian process regression fits are shown (c) and (d) Outer target density profiles as a function of normalized poloidal flux ρ. The large circles and corresponding error bars are the results of a binning procedure on raw data. (e) and (f) Divertor collisionality as a function of ρ. The Λ profiles errors are obtained propagating the errors on density and temperature. Sub-figure (i) refers to AUG whereas sub-figure (ii) refers to TCV.

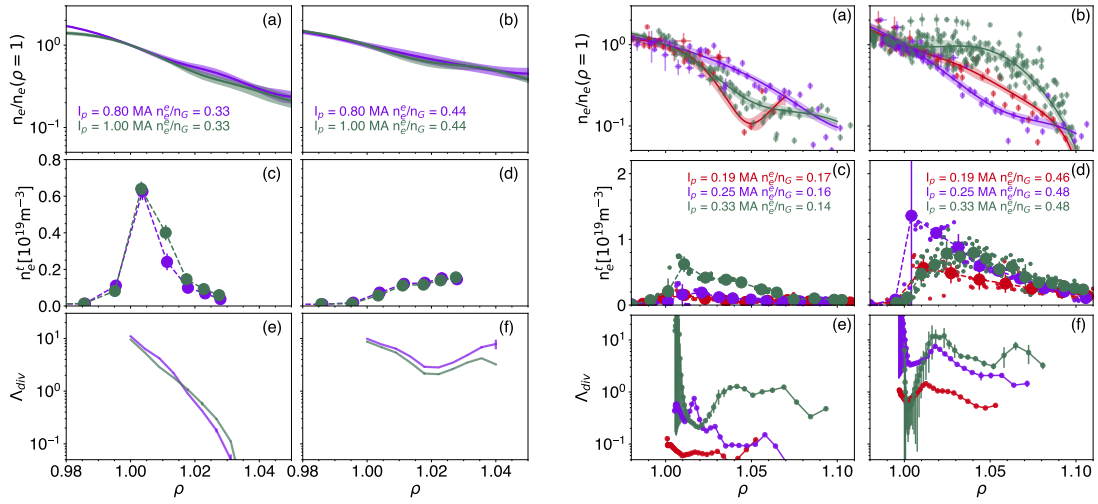

(i) ASDEX Upgrade (ii) TCV

Figure 9: (a) and (b) Upstream density profiles, normalized to the values at the separatrix at different currents levels (colour code) with the same q_{95} at the same level of edge Greenwald fraction. For TCV both the raw data and the Gaussian process regression fit are shown. (c) and (d) Outer target density profiles as a function of normalized poloidal flux ρ. The large circles and corresponding error bar are the results of a binning procedure on raw data. (e) and (f) Divertor collisionality as a function of ρ. The Λ profiles error are obtained propagating the errors on density and temperature. Sub-figure (i) refers to AUG whereas sub-figure (ii) refers to TCV.

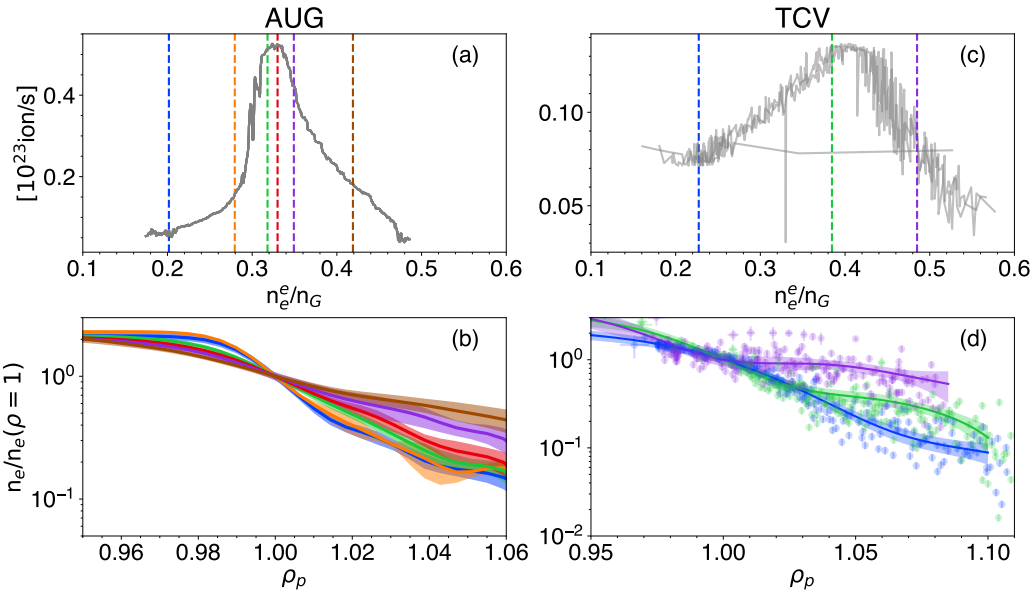

Figure 10: (a) Total integrated ion flux at the outer target as a function of edge density normalize to Greenwald density for AUG. (b) SOL density profile normalized to the density at the separatrix for AUG. The colors refer to the values of density marked in panel (a). (c) Total integrated ion flux to the outer target in TCV as a function of edge density normalized to Greenwald fraction (d) Upstream profiles normalized to the density at the separatrix. The lines indicate the result of a GPR fit whereas the points indicate the actual data. The color code refers to the vertical lines indicated in panel (c).

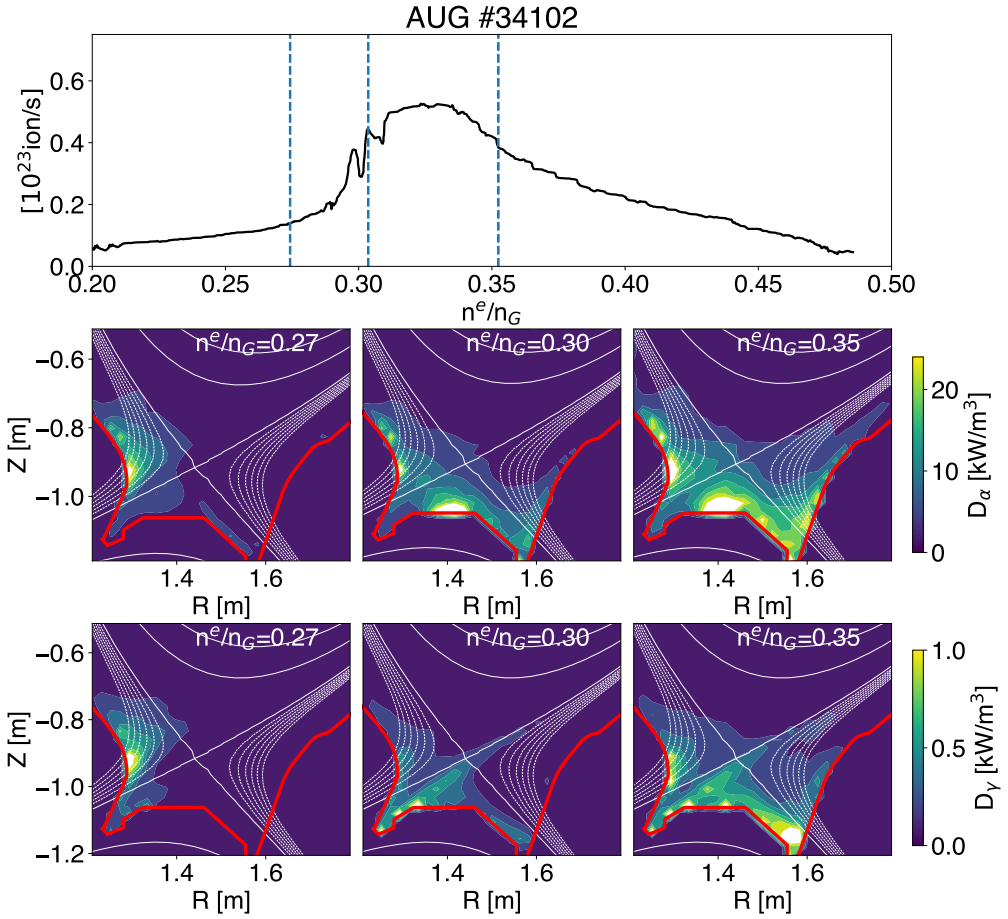

Figure 11: Top panel: Integrated ion flux at the outer target as a function of normalized Greenwald edge density: Middle row: Tomographic inversion of D_α radiation at three different values of n_e^e/n_G. Bottom row: Tomographic inversion of D_γ radiation at three different values of n_e^e/n_G.

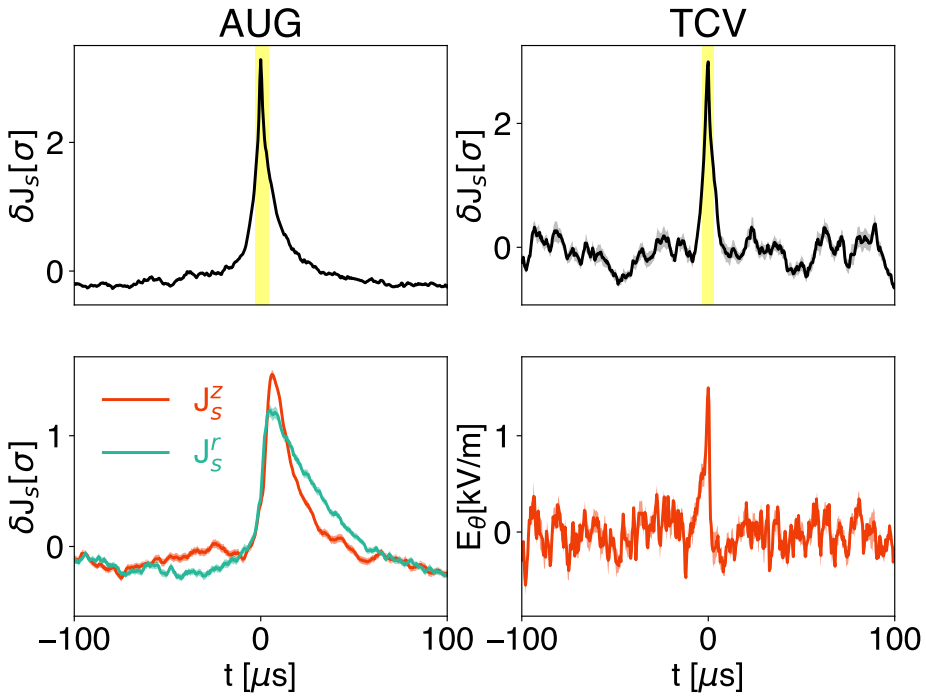

Figure 12: Conditional average samples results as obtained in low-density discharges on AUG (left columns) and TCV (right columns). The condition is the detection of peaks on ion saturation current exceeding 2.5 times the value of the standard deviation above the mean value. The upper panels shows the ion saturation current typical waveform normalized to the standard deviation. The yellow bar indicates the estimate of the FWHM. For AUG the lower panel shows the corresponding Conditionally Sample waveform on the ion saturation current displaced in the radial J_s^r and in the poloidal J_s^Z direction, used in the 2D cross-correlation analysis for the estimate of the binormal velocity. They are both normalized to the respective standard deviation σ. For TCV the waveform on the poloidal electric field fluctuation is associated to the ion saturation blob. It is worth remembering that on TCV the radial velocity fluctuations is estimated from local poloidal electric field fluctuations as explained in the text.

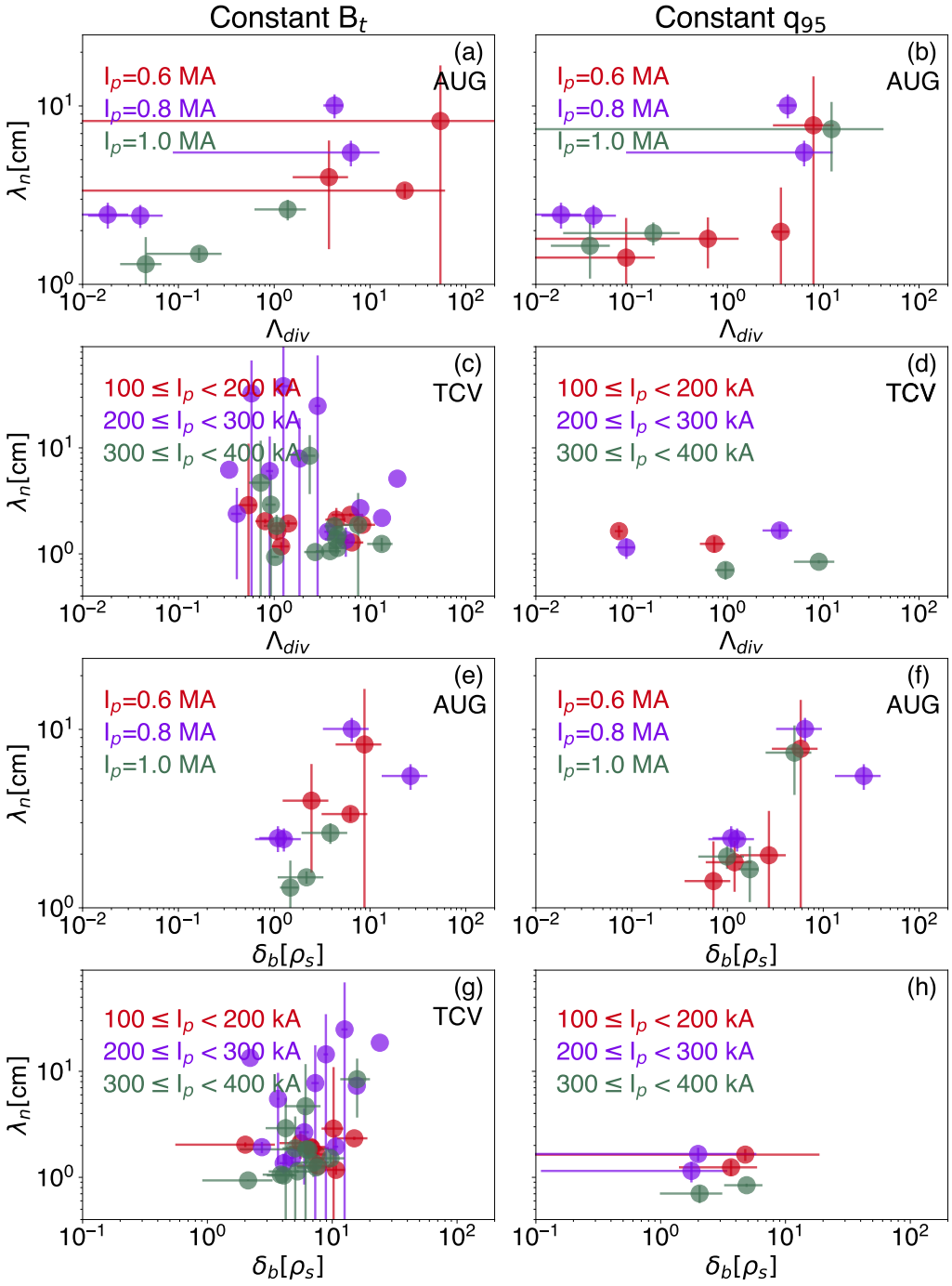

Figure 13: SOL density e-folding length λ_n *vs* outer divertor collisionality Λ_{div} for the scan at constant B_t (a) and at constant q_{95} (b) on AUG. λ_n *vs* Λ_{div} for the scan at constant B_t (c) and at constant q_{95} (d) for TCV . SOL density e-folding length λ_n *vs* blob-size δ_b for the scan at constant B_t (e) and at constant q_{95} (f) on AUG. (c) λ_n *vs* δ_b for the scan at constant B_t (g) and at constant q_{95} (h) on TCV. Different colours refer to different currents. The errors on Λ are obtained from the propagation of density and temperature errors. The errors on λ_n are obtained propagating the error on the gradient estimate and the density profile fit estimate. The errors on blobs are estimated propagating the errors on τ_b as well as the errors on velocities. These have been computed considering the error on the shape of the conditionally average sample waveforms.

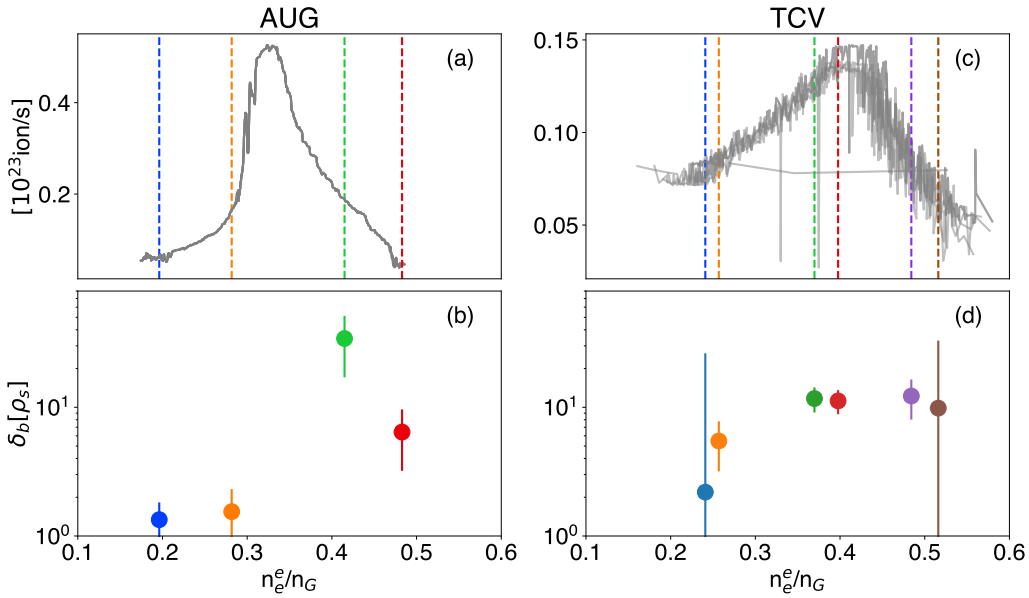

Figure 14: (a) Total integrated ion flux at the outer target as a function of edge density normalized to Greenwald density for AUG. (b) Blob-size as a function of edge density normalized to Greenwald density on AUG. The colours refer to the values of density marked in panel (a). (c) Total integrated ion flux to the outer target in TCV as a function of edge density normalized to Greenwald fraction (d) Blob-size as a function of edge density normalized to Greenwald density on TCV.The error on blobs are estimated propagating the error on τ_b as well as the errors on velocities. These have been computed considering the error on the shape of the conditionally averaged sample waveforms.

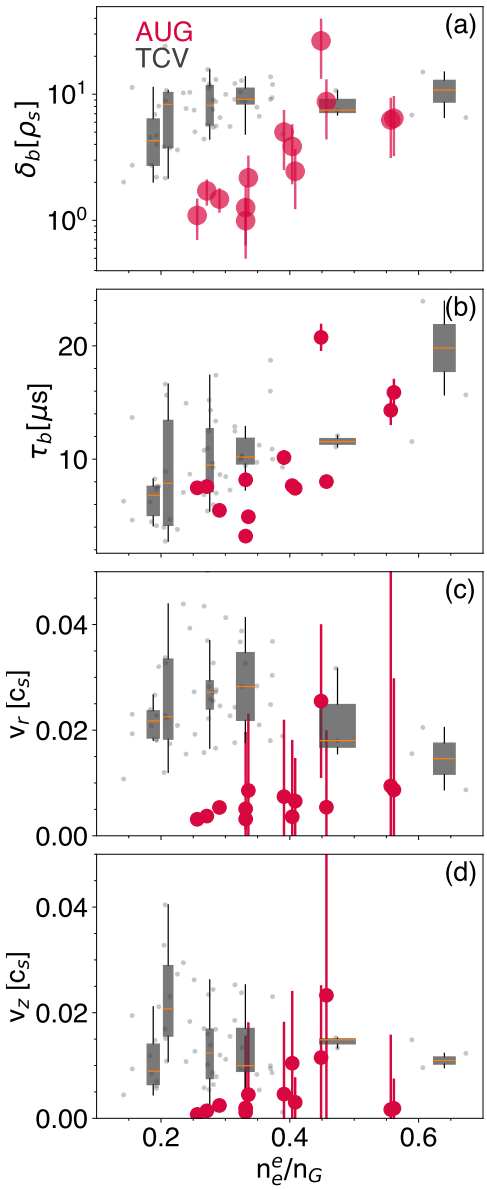

Figure 15: (a) Blob-size as a function of edge Greenwald fraction for AUG and TCV. (b) τ_b as a function of edge Greenwald fraction. (c) Radial velocity normalized to ion sound speed as a function of edge Greenwald fraction. (d) Poloidal velocity as a function of edge Greenwald fraction. For TCV in order to highlight the trend the data have been binned in classes of n_e/n_G, and the corresponding box-plot are shown, with boxes representing 50 % of the population, and the orange lines representing the median of the distribution of the bin. The center of the box is positioned at the median value of the corresponding density population.

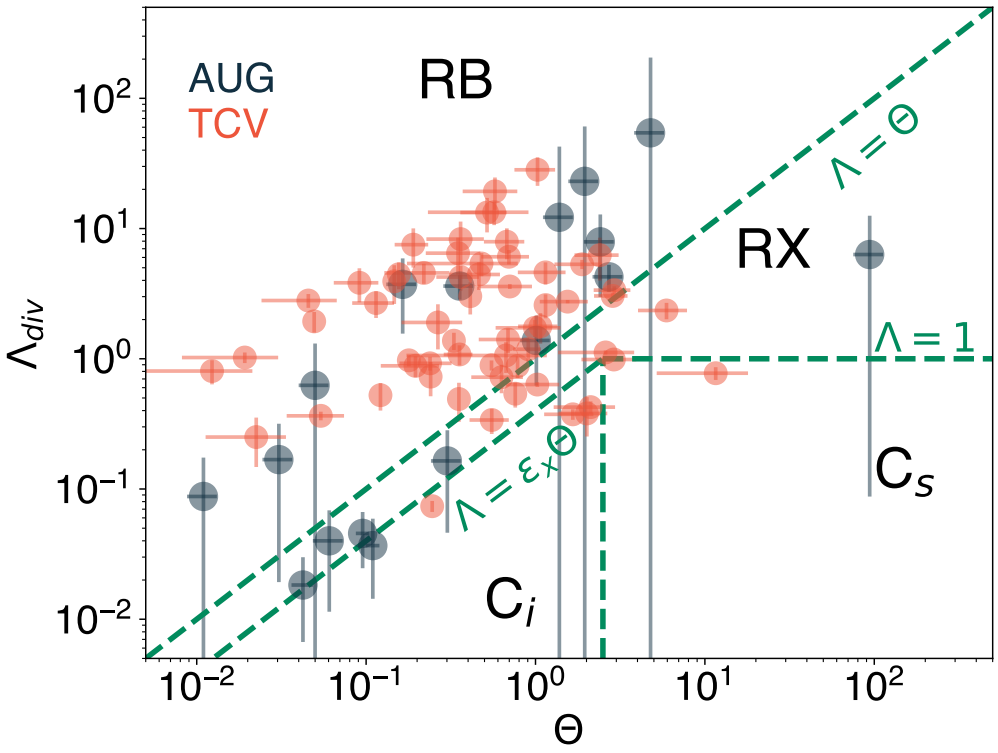

Figure 16: Λ_{div} vs Θ for L-Mode discharges in TCV and ASDEX Upgrade. The different regimes C_s (sheath-connected), C_i (connected ideal interchange), RX (resistive X-point) and RB (resistive ballooning) are marked. In the plot we have used a magnetic fanning parameter $\epsilon_x = 0.3$. The error bars on Λ are obtained propagating the errors on target density and temperature. The errors on Θ are obtained from the error on blobs which are estimated propagating the error on τ_b as well as the errors on velocities. These have been computed considering the error on the shape of the conditionally averaged sample waveforms.

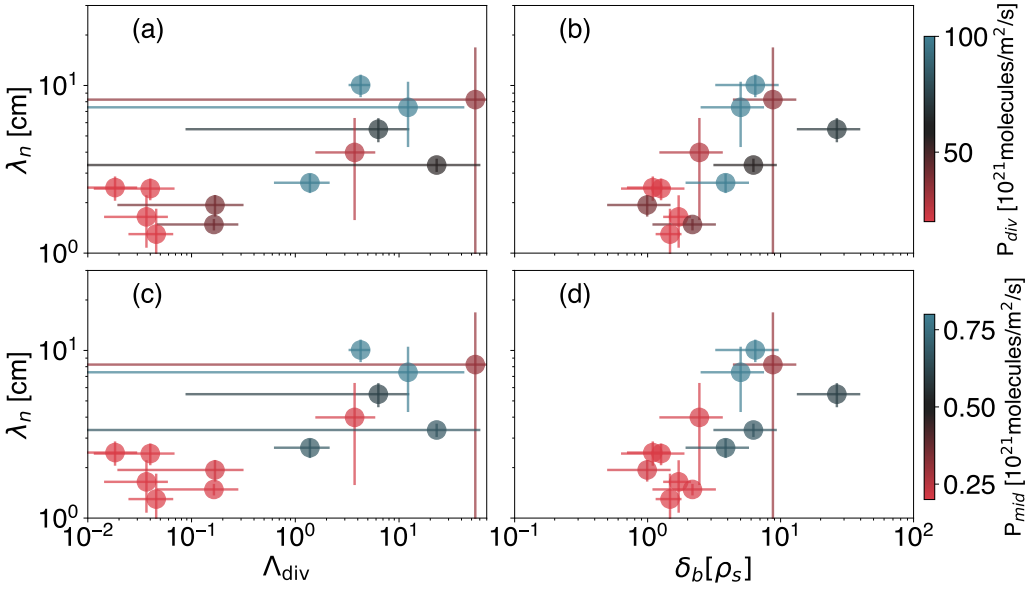

Figure 17: (a) λ_n *vs* Λ_{div} with colour code proportional to divertor pressure. (b) λ_n *vs* δ_b with colour code proportional to divertor pressure. (c) λ_n *vs* Λ_{div} with colour code proportional to midplane pressure. (d) λ_n *vs* δ_b with colour code proportional to midplane pressure. All data refer to AUG.The errors on blobs are estimated propagating the errors on τ_b as well as the errors on velocities. These have been computed considering the errors on the shape of the conditionally average sample waveforms. The errors on λ_n are obtained propagating the errors on the gradient estimate and the density profile fit estimate.

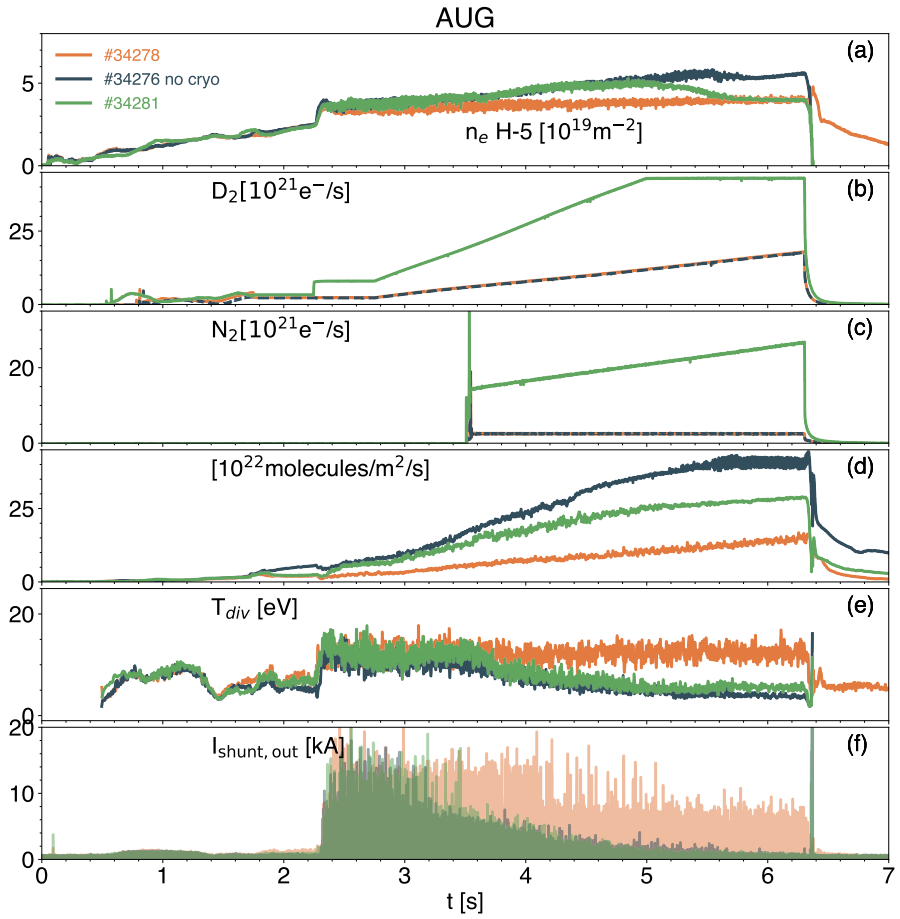

Figure 18: (a) Edge density from H-5 interferometer chord (b) Total deuterium fuelling (c) Total nitrogen seeding (d) Sub-divertor neutral pressure (e) Temperature at the outer target (f) Shunt current at the outer target used as a proxy for ELM detection. The colours refer to three different discharges, all with the same heating power. In discharge # 34276 the cryogenic pump was not in operation.

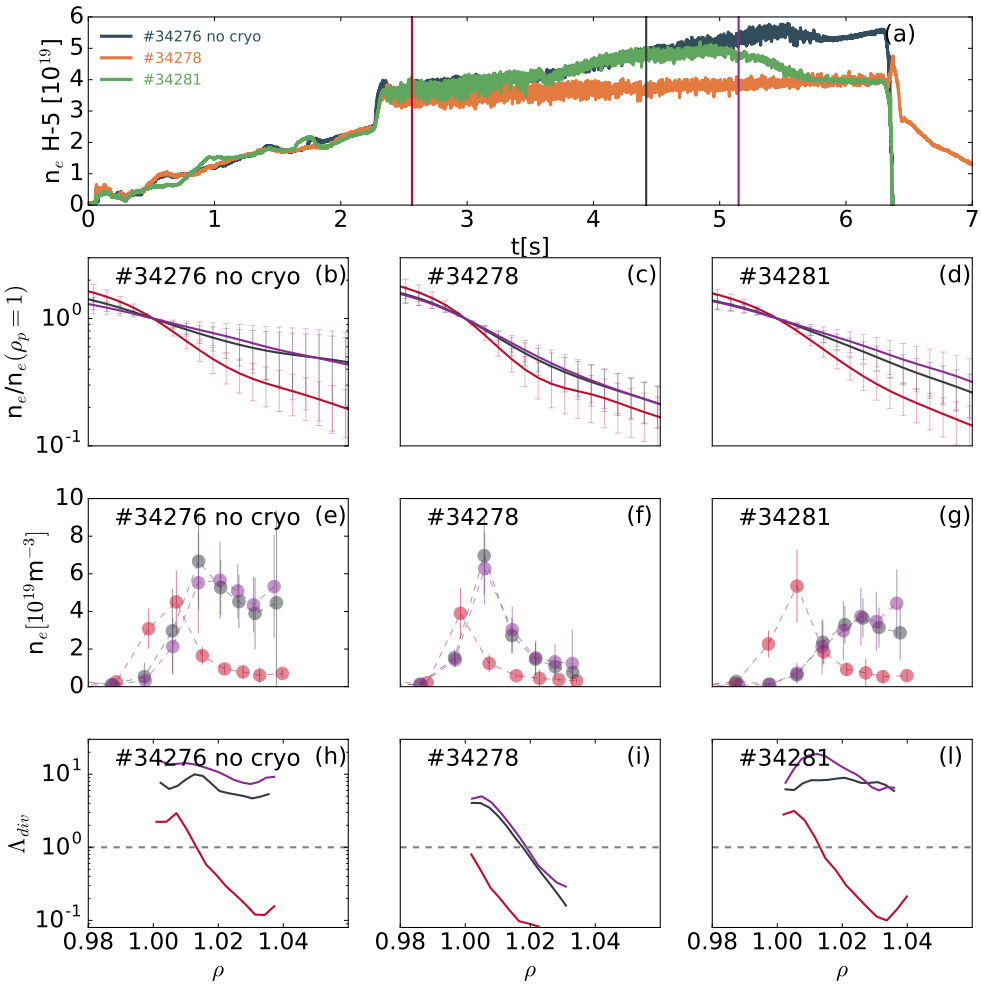

Figure 19: (a) Edge density vs time for the shots #34276 (no cryogenic pump), #34278 and #34281 (b-d). Inter-ELM upstream density profiles normalized to values at the separatrix respectively for shots 34276, 34278 and 34281. The different colours refer to different time instants marked in panel (a).(e-g) Inter-ELM target density profiles for the 3 shots at the same time instants as previous row (h-l) inter-ELM Λ_{div} profiles. Only ASDEX Upgrade data are presented.

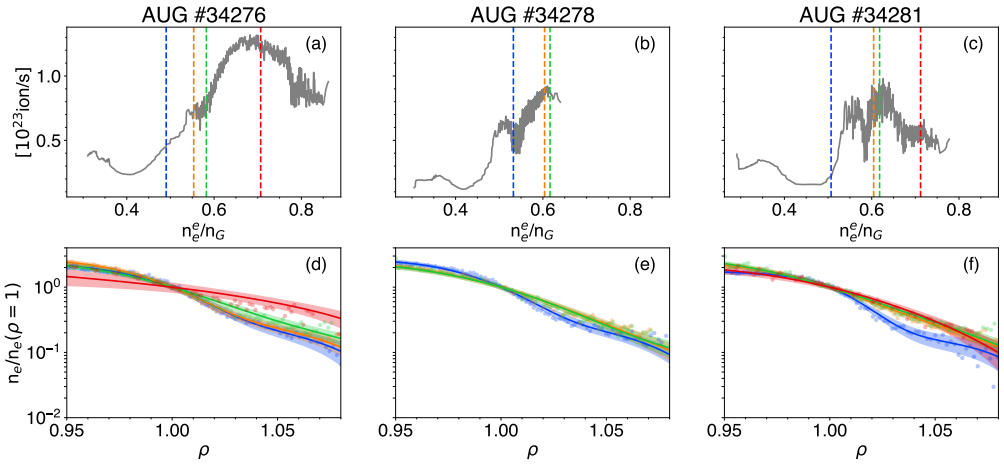

Figure 20: (a-c) Total outer divertor integrated ion flux vs edge density normalized to Greenwald fraction. The vertical colour lines refer to the chosen interval for the evaluation of upstream profiles (d-f). Upstream profile normalized to the value at the separatrix at different values of normalized edge Greenwald fraction. All data refer to AUG H-Mode operation.

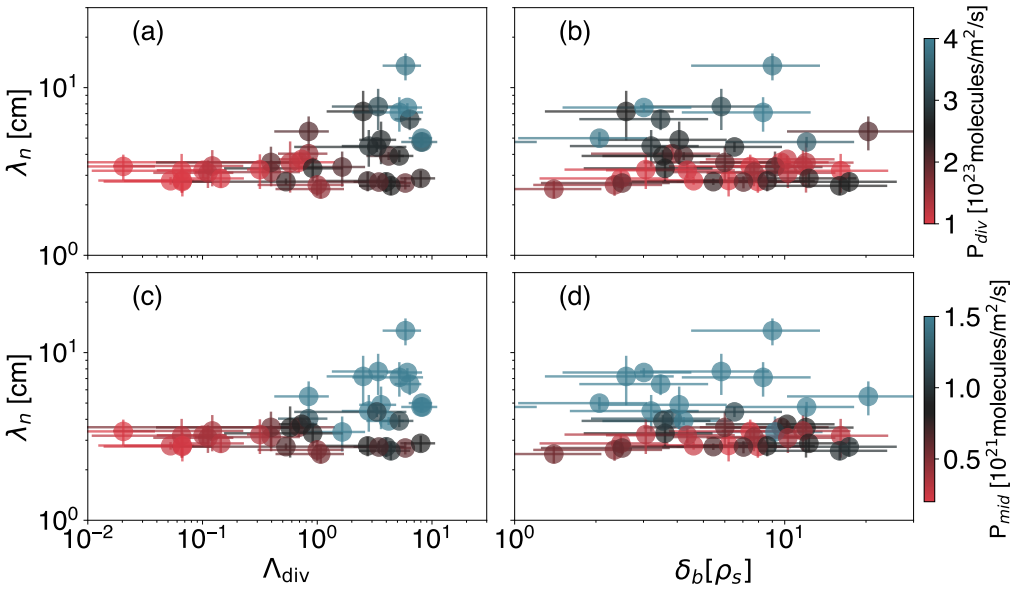

Figure 21: (a) SOL density e-folding length λ_n *vs* edge collisionality $\Lambda_{\rm div}$ with colour code proportional to divertor pressure. (b) e-folding length λ_n *vs* blob-size δ_b with colour code proportional to divertor pressure. (c) λ_n *vs* $\Lambda_{\rm div}$ with colour code proportional to midplane pressure. (d) λ_n *vs* δ_b with colour code proportional to midplane pressure. All data refer to AUG H-mode operation. The errors on blobs are estimated propagating the errors on τ_b as well as the errors on velocities. These have been computed considering the errors on the shape of the conditionally average sample waveforms. The errors on λ_n are obtained propagating the errors on the gradient estimate and the density profile fit estimate.

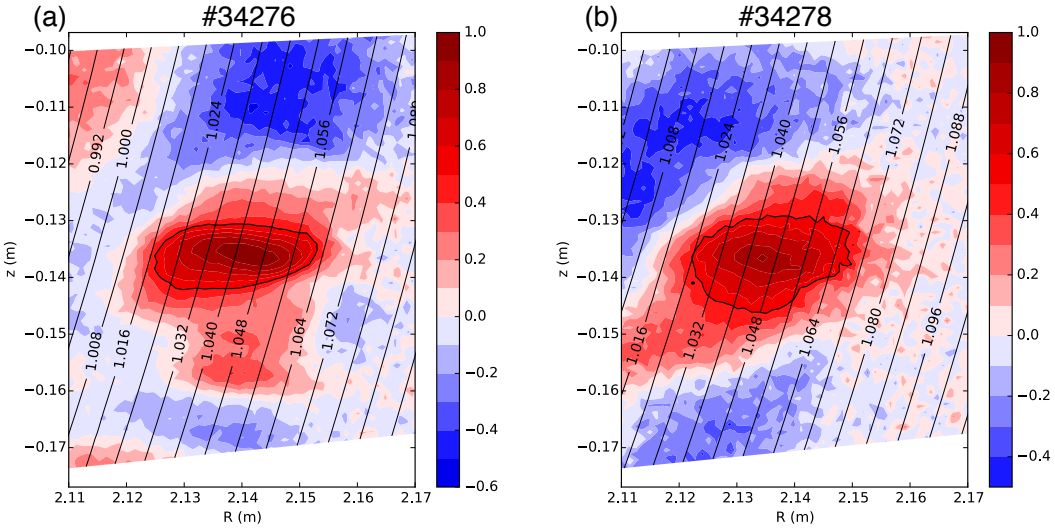

Figure 22: (a) Inter-ELM blob as measured through cross-correlation technique for shot # 34276 in the period 4.368 s. (b) inter-ELM blob as measured through cross-correlation technique for shot # 34278 in the period 2.513-2.613 s. The solid back contour indicates the contour line of 0.5 correlation value. The flux surface labels are indicated as well.